Cohesin depleted cells pass through mitosis and reconstitute a functional nuclear architecture

Marion Cremer[1,*,§], Katharina Brandstetter[2,*], Andreas Maiser[2], Suhas S P Rao[3,4], Volker Schmid[5], Namita Mitra[3], Stefania Mamberti[6], Kyle-N Klein[7], David M Gilbert[7], Heinrich Leonhardt[2], Maria Cristina Cardoso[6], Erez Lieberman Aiden[3,8,9,10], Hartmann Harz[2,§], Thomas Cremer[1,§]

1. Anthropology and Human Genomics, Department Biology II, Ludwig-Maximilians-Universität München, Germany
2. Human Biology & BioImaging, Center for Molecular Biosystems, Department Biology II, Ludwig-Maximilians-Universität München, Germany
3. Center for Genome Architecture, Department of Molecular and Human Genetics, Baylor College of Medicine, Houston, Texas, United States of America
4. Department of Structural Biology, Stanford University School of Medicine, California, United States of America
5. BioImaging Group, Department of Statistics, Ludwig-Maximilians-Universität München, Germany
6. Cell Biology and Epigenetics, Department of Biology, Technische Universität Darmstadt, Germany
7. Department of Biological Science, Florida State University, Tallahassee, Florida, United States of America
8. Center for Theoretical Biological Physics, Rice University, Houston, Texas, United States of America
9. Broad Institute of the Massachusetts Institute of Technology and Harvard University, Cambridge, Massachusetts, United States of America
10. Departments of Computer Science and Computational and Applied Mathematics, Rice University, Houston, Texas, United States of America

*equal contribution, § corresponding authors

Abstract

The human genome forms thousands of “contact domains”, which are intervals of enhanced contact frequency. Some, called “loop domains” are thought to form by cohesin-mediated loop extrusion. Others, called “compartmental domains”, form due to the segregation of active and inactive chromatin into A and B compartments. Recently, Hi-C studies revealed that the depletion of cohesin leads to the disappearance of all loop domains within a few hours, but strengthens compartment structure. Here, we combine live cell microscopy, super-resolution microscopy, Hi-C, and studies of replication timing to examine the longer-term consequences of cohesin degradation in HCT-116 human colorectal carcinoma cells, tracking cells for up to 30 hours. Surprisingly, cohesin depleted cells proceed through an aberrant mitosis, yielding a single postmitotic cell with a multilobulated nucleus. Hi-C reveals the continued disappearance of loop domains, whereas A and B compartments are maintained. In line with Hi-C, microscopic observations demonstrate the reconstitution of chromosome territories and chromatin domains. An interchromatin channel system (IC) expands between chromatin domain clusters and carries splicing speckles. The IC is lined by active chromatin enriched for RNA Pol II and depleted in H3K27me3. Moreover, the cells exhibit typical early-, mid-, and late- DNA replication timing patterns. Our observations indicate that the functional nuclear compartmentalization can be maintained in cohesin depleted pre- and postmitotic cells. However, we find that replication foci – sites of active DNA synthesis – become physically larger consistent with a model where cohesin dependent loop extrusion tends to compact intervals of replicating chromatin, whereas their genomic boundaries are associated with compartmentalization, and do not change.

Abbreviations

3D FISH = 3D fluorescence in situ hybridization
3D SIM = 3D structured illumination microscopy
AID = auxin inducible degron
ANC / INC = active / inactive nuclear compartment
CT = chromosome territory
CD(C) = chromatin domain (cluster)
CTCF = CCCTC binding factor
DAPI = 4',6-diamidino-2-phenylindole
EdU = 5-Ethynyl-2'-deoxyuridine
Hi-C = chromosome conformation capturing combined with deep sequencing
IC = interchromatin compartment
MLN = multilobulated nucleus
NC = nucleosome cluster
PBS = phosphate buffered saline
PBST = phosphate buffered saline with 0.02% Tween
PR = perichromatin region
RD = replication domain
RL = replication labeling
TAD = topologically associating domain

Introduction

Cohesin, a ring-like protein complex with its major subunits RAD21, SMC1 and SMC3 is involved in numerous nuclear processes, such as in double strand break repair and gene regulation, by exerting its key function of tethering distant genomic loci [1-7]. In addition, cohesin entraps sister chromatids to ensure faithful chromosome segregation during mitosis (reviewed in [1]).

In recent years cohesin's ability as shaper of chromatin loops in the sub-Mb range anchored at CTCF/cohesin binding sites [8, 9] has moved into the spotlight of research. Hi-C studies have indicated that these loops, which manifest as bright peaks in contact frequency in a Hi-C map, demarcate contact domains [10, 11]. They manifest as squares of enhanced contact frequency in a Hi-C map and correspond to self-interacting genomic intervals between 50kb and 1Mb where DNA sequences physically interact with each other more frequently compared to sequences outside a given domain [12, 13]. Loop domains thus comprise a structural unit of chromatin organization [14, 15].

Studies on the impact of cohesin in nuclear functions have become highly facilitated by an approach, which triggers a rapid and selective proteolysis of RAD21 by integrating an auxin-inducible degron (AID) system and its fusion to both endogenous RAD21 alleles into a given cell line [16] (for review see [17]). Addition of auxin results in RAD21 proteolysis with the concomitant disintegration of cohesin from chromatin [18].

Using this system in the colon cancer derived HCT116-RAD21-mAC cell line, we recently demonstrated the rapid disappearance of loop domains in Hi-C contact matrices averaged over large cell populations [18]. Compartments, manifesting when chromatin intervals with common histone signatures co-localize [13], were retained and even strengthened, leading to the presence of compartment domains and even compartment loops (but no loop domains) in the treated cells [18]. Other studies, using different cell types and approaches for cohesin elimination yielded similar results [19-21], (reviewed in [22]).

Here, we study the longer-term consequences of cohesin depletion and its effects on the higher order nuclear architecture via a combination of super-resolution and live cell microscopy, as well as Hi-C and Repli-Seq. We found that cohesin depleted interphase cells

proceed through a greatly prolonged mitosis resulting in a single cell with one multilobulated nucleus (MLN) after chromatid segregation. With Hi-C we confirm both the continued disappearance of loop domains and the maintenance of A and B compartments in MLN. With super-resolved microscopy we demonstrate that nuclei of pre- and postmitotic cohesin depleted cells maintain principal structural features of the ANC-INC model (reviewed in [23-25]). According to this model, which has been supported by electron microscopy and 3D super-resolution fluorescence microscopic studies from various species and cell types, the global nuclear landscape is shaped by chromosome territories (CTs) built up from chromatin domains (CDs) and chromatin domain clusters (CDCs). CDCs show a multilayered shell-like organization with increasing chromatin compaction levels from the periphery toward the interior CDC core. An interconnected system of interchromatin channels, called the interchromatin compartment (IC), pervades the spaces between CDCs. The IC carries splicing speckles and nuclear bodies within IC-lacunas and plays a central role in the formation of various nuclear machineries. IC-channels penetrate the layer of heterochromatin beneath the nuclear envelope and form direct contacts with nuclear pore complexes. The IC is lined by CDs with less compacted chromatin, first described in electron microscopic studies as the perichromatin region (for review see [26]). The PR serves as the preferential nuclear subcompartment for transcription and co-transcriptional splicing. The IC and PR form the active nuclear compartment (ANC), whereas CDs with a more compact, ‘closed’ chromatin configuration are located further away from the IC and comprise the INC.

We also examined replication timing, which has been linked to domain structure [27]. Strikingly, the absence of cohesin did not lead to major changes in replication timing or in the genomic extent of replication domains (RDs), indicating that the two structures form by independent mechanisms. Instead, we find that the boundaries of RDs closely match those of the A and B compartments both before and after cohesin degradation. This matches the Repli-Seq findings reported in [28] and is consistent with the observation of [29]. Taken together, our findings indicate that replication domains correspond with compartment domains, but not with loop domains. However, we find that the physical size of replication foci is smaller, suggesting that cohesin-depending extrusion may play a role in the physical compaction of replicating

chromatin.

Results

Validation of auxin induced proteolysis of the cohesin subunit RAD21

All experiments of this study were performed with the human colon cancer derived cell line HCT116-RAD21-mAC [16], where an auxin-inducible degron (AID) is fused to both endogenous RAD21 alleles and to a fluorescent reporter (see Suppl_Fig.1). The complete loss of RAD21-mClover fluorescence was seen in live cell observations ~1:30h after incubation in 500 µM auxin (Suppl_Fig.2A). Degradation of RAD21 was confirmed by negative immunostaining with a RAD21 antibody, while epitopes of cohesin subunits SMC1 and SMC3 remained intact under auxin shown by persisting positive immunodetection with respective antibodies (Suppl_Fig.2B). Notably, a small fraction of cells in our cultures (~2-4%) escaped auxin induced RAD21 degradation. In order to exclude non-responsive cells from further analyses of the impact of cohesin depletion, RAD21-mClover fluorescence was routinely recorded in all experiments with auxin treated cell populations except for 3D-FISH experiments since DNA heat denaturation destroys the reporter fluorescence [30].

Cohesin depletion leads to delayed mitosis and final transition into a single postmitotic cell with a multilobulated nucleus (MLN)

Using time lapse imaging over 21h at Δt=15min, we compared in parallel entrance into mitosis, mitotic progression and exit in untreated controls and in cohesin depleted HCT116-RAD21-mAC cells, where auxin was added just before starting life cell observations. In control cells (Fig. 1A) ~80% of all recorded mitoses (n=45) passed mitosis within <1h and formed two inconspicuous daughter nuclei. A second mitosis observed for individual nuclei ~20h after the first division demonstrates their capacity to divide again under the given observation conditions. Notably, about 20% of mitoses recorded in untreated control cells revealed prolonged mitoses of >2h followed by transition into an abnormal cell nucleus, a feature which is not unusual in tumor cell lines (reviewed in [31]). Mitotic entrance of auxin treated cells

(n=32) did not show any conspicuous differences to controls (Fig.1B). However, their passage through mitosis was consistently delayed up to 14h (median 4.5h). This prolonged mitotic stage raised the mitotic index in cohesin depleted cell cultures fixed after 6h in auxin to almost 30% versus ~4% in control cultures (Suppl_Fig.3). The delayed mitotic passage was associated with the formation of abnormal multipolar mitotic figures persisting over several hours. Fig. 1C depicts a typical telophase stage of ~30 min with two apparent daughter nuclei preceding the formation of a single MLN. Despite their seemingly separation, these daughter nuclei, however, were presumably still connected by filaments (see below) and did not enter into cytokinesis. Instead, all cohesin depleted cells that were followed through an entire mitosis (n=19) resulted in a single MLN (Fig.1B-C). As a consequence, in cell cultures fixed 28-30h after cohesin depletion, MLN accumulated up to ~60% versus ~2% in control cultures (Suppl_Fig.3). MLN were noted in cell cultures kept up to 50h where a considerable fraction of apoptotic cell nuclei indicated their decline (data not shown).

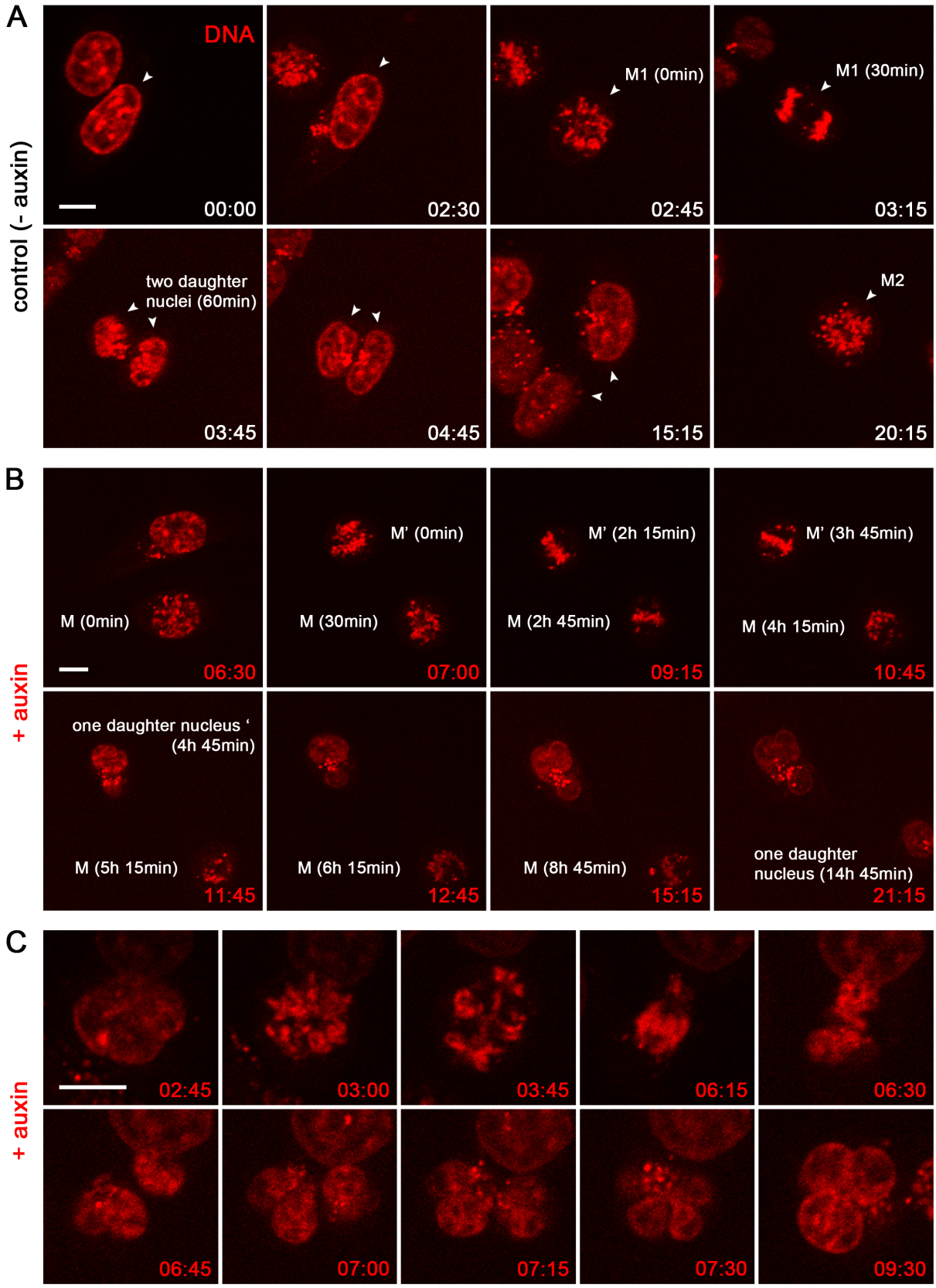

Fig. 1: Live cell microscopy demonstrating highly prolonged abnormal mitosis and subsequent formation of one multilobulated nucleus (MLN) in cohesin depleted cells

(A) Selected points from time lapse imaging (∑t=21h, Δt=15min) of untreated control cells (DNA stained with SiR-DNA, red) with accomplishment of mitosis (M1) within 1h (time 02:45 – 03:45) and

subsequent formation of two daughter nuclei. A second mitosis (M2) of one daughter nucleus is shown at time 20:15**. (B)** Selected time lapse images of nuclei after cohesin degradation conducted in parallel to control cells demonstrate a prolonged mitotic stage. Mitosis (M) emerges at time 6:30 after auxin treatment, transition into one abnormal multilobulated daughter nucleus (MLN) is seen 14:45h later (time 21:15). Mitosis (M') emerges 7h after auxin treatment (time 07:00), transition into an MLN is seen 4:45h later (time 11:45). **(C)** Time lapse imaging from the same series at a higher zoom shows the formation of an aberrant mitosis apparently reaching telophase at time 6:30. 15 min later two seemingly separated daughter nuclei, presumably connected by filaments, become fused into one MLN at time 7:15. Scale bar: 10 µm

Global features of higher order chromatin organization persist after cohesin depletion and are re-established in MLN after mitosis despite the loss of loop domains

Maintenance and re-formation of chromosome territories (CTs)

Maintenance of a territorial organization of interphase chromosomes in cohesin depleted cell cultures was tested by chromosome painting of CTs 4, 12 and 19 (Fig. 2). In line with the near-diploid karyotype of HCT116 cells [32, 33], two homologous territories of each painted chromosome were detected in interphase nuclei of both control (Fig. 2A) and cohesin depleted cells fixed after 6h auxin treatment (Fig. 2B). Segregation of chromatids in cohesin depleted cells was noted in anaphase (Fig. 2C, mid). Accordingly, a substantial fraction of postmitotic MLN revealed four painted territories often located in different lobuli (Fig. 2D). Unexpectedly, chromosome painting, however, detected also MLN with more than four variably sized painted segments for a given painted chromosome (Fig. 2E and Suppl_Fig. 4). Arguably, chromatids were torn apart by mechanic forces during an aberrant anaphase and/or during lobe formation. This disruption was possibly enhanced by a higher level of relaxation / decondensation in cohesin depleted chromatin (see below).

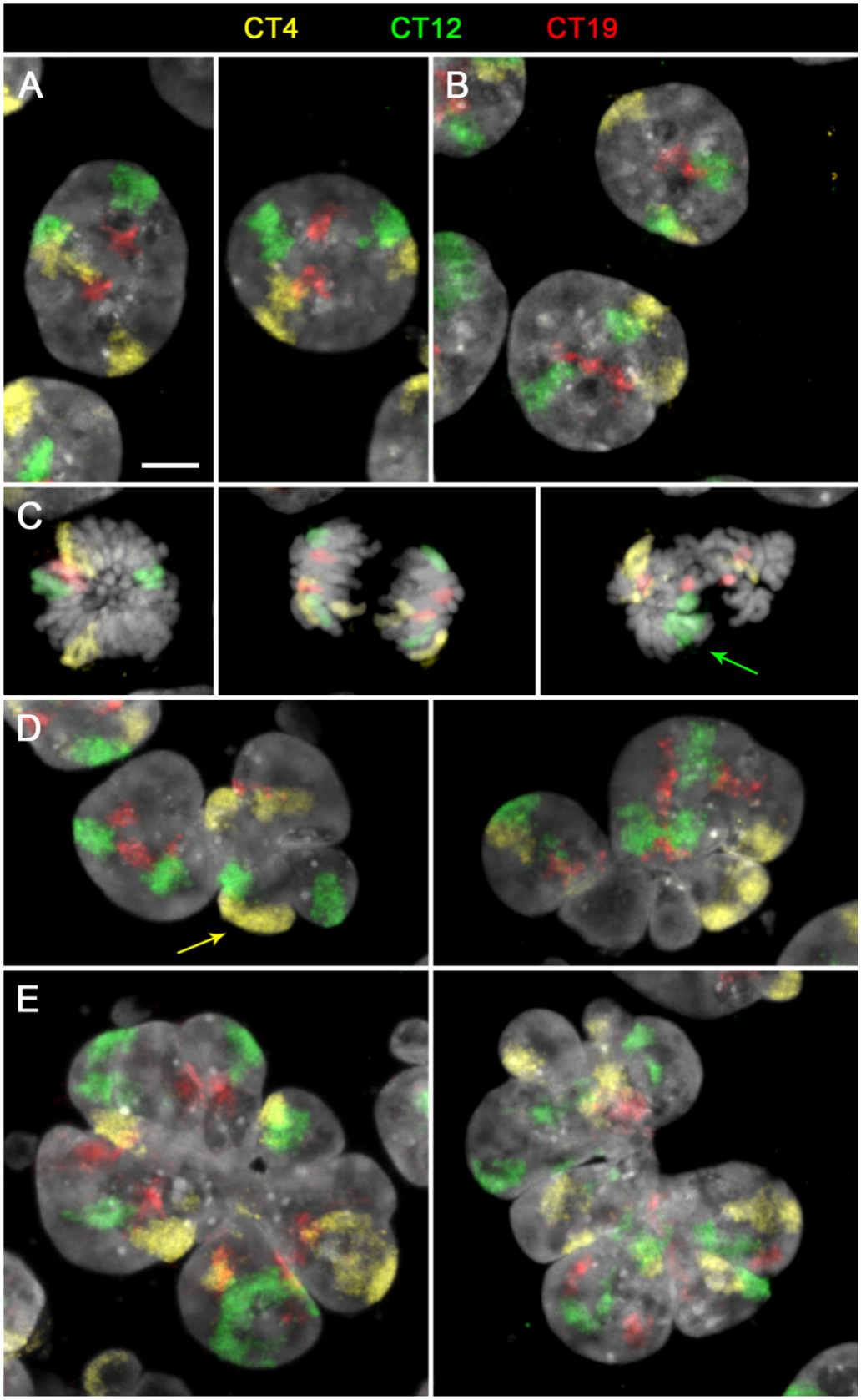

Fig. 2: Maintenance of chromosome territories (CTs) in cohesin depleted nuclei and their re-establishment after mitosis

(A-E) Z-projections of entire DAPI stained nuclei (gray) with painted territories of chromosomes 4 (yellow), 12 (green) and 19 (red) acquired by confocal fluorescence microscopy. **(A)** Control nuclei

and **(B)** cohesin depleted premitotic nuclei with normal phenotypes after 6h in auxin show two inconspicuous copies for each CT. **(C)** Mitoses from 6h auxin treated cultures with two coherent chromosomes in an (early) metaphase plate *(left),* segregated chromatids in anaphase *(mid)* and missegregation of chromosome 12 (arrow) in an abnormal mitotic figure *(right)*. **(D)** Postmitotic multilobulated nuclei (MLN) with four copies for each CT. Arrow marks two CTs 4 that cannot be distinguished in the z-projection. **(E)** MLN with >4 painted regions for each CT (compare also Suppl_Fig. 4). Scale bar: 5 µm

Maintenance of co-aligned functionally interacting active and inactive nuclear compartments (ANC-INC) in nuclei of cohesin depleted pre- and postmitotic cells

3D structured illumination microscopy (3D-SIM) revealed similar chromatin compaction patterns both in DAPI stained control and cohesin depleted nuclei, including postmitotic MLN. This and other findings described below provide evidence for major structural and functional features of the ANC-INC model (Fig. 3 and 4, and introduction). For a quantitative analysis of nuclear serial sections, DAPI fluorescence was divided into seven intensity classes with equal intensity variance (color code in Fig.3). This representation of nuclear landscapes as color heat maps with increasing DNA densities (Fig 3 A-C) served as proxy for classes with increasing chromatin compaction [34]. Class 1 (lowest DNA density) represents the interchromatin compartment (IC), classes 2 (and 3) comprise low compaction CDs lining the IC. At the nuclear periphery IC-channels expand between lamina associated domains toward nuclear pores (Fig. 3D-F). The quantitative assessment of voxels attributed to the seven DAPI intensity classes showed a slight shift towards less compacted chromatin (classes 1 and 2) in cohesin depleted nuclei compared to controls (Fig. 3G), in line with a slight increase of nuclear volumes after 6h cohesin depletion. The ~2-fold increased nuclear volume in MLN (30h auxin) reflects the double amount of DNA in these postmitotic cells. (Fig. 3H).

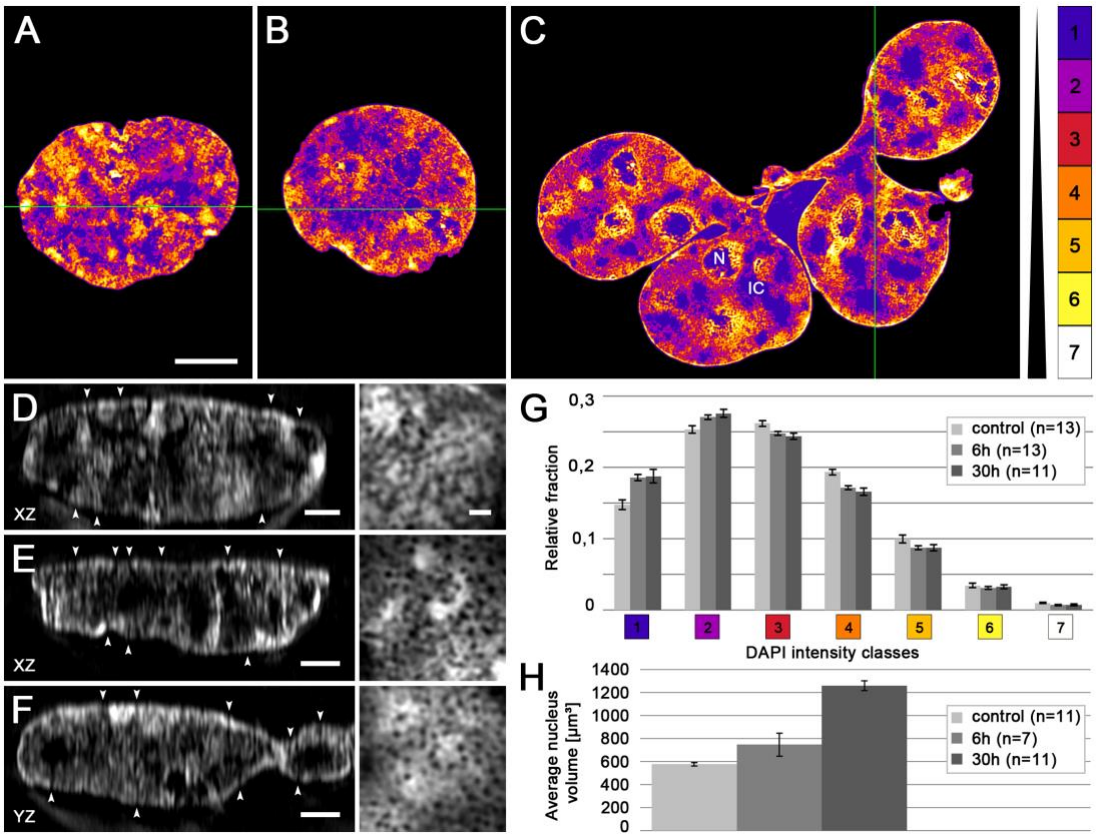

Fig. 3: Topological chromatin compaction mapping

(A-C) DAPI stained mid-sections of representative nuclei acquired by 3D-SIM from **(A)** control nucleus; **(B)** Cohesin depleted nucleus (6h auxin); **(C)** Cohesin depleted multilobulated nucleus (MLN) (30h auxin). Chromatin compaction of nuclei based on seven DAPI intensity classes is displayed in false colors. Class 1 (*blue*) represents pixels close to background intensity, largely reflecting the interchromatin compartment (IC), class 7 (*white*) pixels with highest intensities. All nuclei in A-C reveal a network of chromatin domain clusters (CDCs) comprising a compacted core and a surrounding low-density layer co-aligned with class 1 regions that meander between CDCs as part of the IC. Likewise, all nuclei display a rim of compacted (hetero)chromatin at the nuclear periphery and around nucleoli. N = nucleolus; IC = interchromatin channels/lacunae. The green lines indicate the section plane for xz/yz cross sections of the respective nuclei shown in (D-F). Scale bar: 5 µm. **(D-F)***(left column):* cross sections from nuclei shown in (A-C) demonstrate connections from the IC with nuclear pores (arrowheads); *(right column):* nuclear pores from respective nuclei shown in apical z–sections. Scale bars: 2 µm in cross sections; 0.5 µm in apical z-sections; **(G)** Relative 3D signal distributions of DAPI intensity classes in control nuclei, in 6h auxin treated nuclei and 30h auxin treated MLN reveal an overall similar profile for each series, yet with a relative increase of classes 1 and 2 ($p<0.05$ for control vs 6h and 30h auxin) and a relative decrease of classes 3 and 4 ($p<0.05$ for control vs 6h and 30h auxin) in cohesin depleted nuclei. *Error bars*= standard error of the mean (SEM) **(H)** Average nuclear volumes from the same series of nuclei show an increase of nuclear volumes after cohesin depletion. Note that MLN after 30h auxin are assumed to contain the double DNA amount compared to controls (for statistical tests and significance see Suppl_Table 1).

For a quantitative mapping of functionally relevant markers on DAPI intensity classes, we performed immunostaining of SC35, an integral protein of splicing speckles, involved in co-transcriptional splicing and transcriptional elongation [35, 36], of RNA Pol II, phosphorylated at Ser5, representing the transcription initiating form of RNA Pol II [37], and of histone H3K27me3 conveying a repressed chromatin state [38] (Fig. 4). SC35 was greatly enriched in the IC (intensity class1), while H3K27me3 chromatin was preferentially located in higher compacted CDs of both controls and cohesin depleted nuclei (Fig. 4A-C). RNA Pol II was enriched in the PR, i.e. decondensed chromatin lining the IC (Fig. 4D-F). Notwithstanding the significantly different distributions of SC35, RNA Pol II and H3K27me3 with regard to the seven DAPI intensity classes, a highly similar distribution was found for each marker both in controls and pre- and postmitotic cohesin depleted cells (Fig. 4G,H).

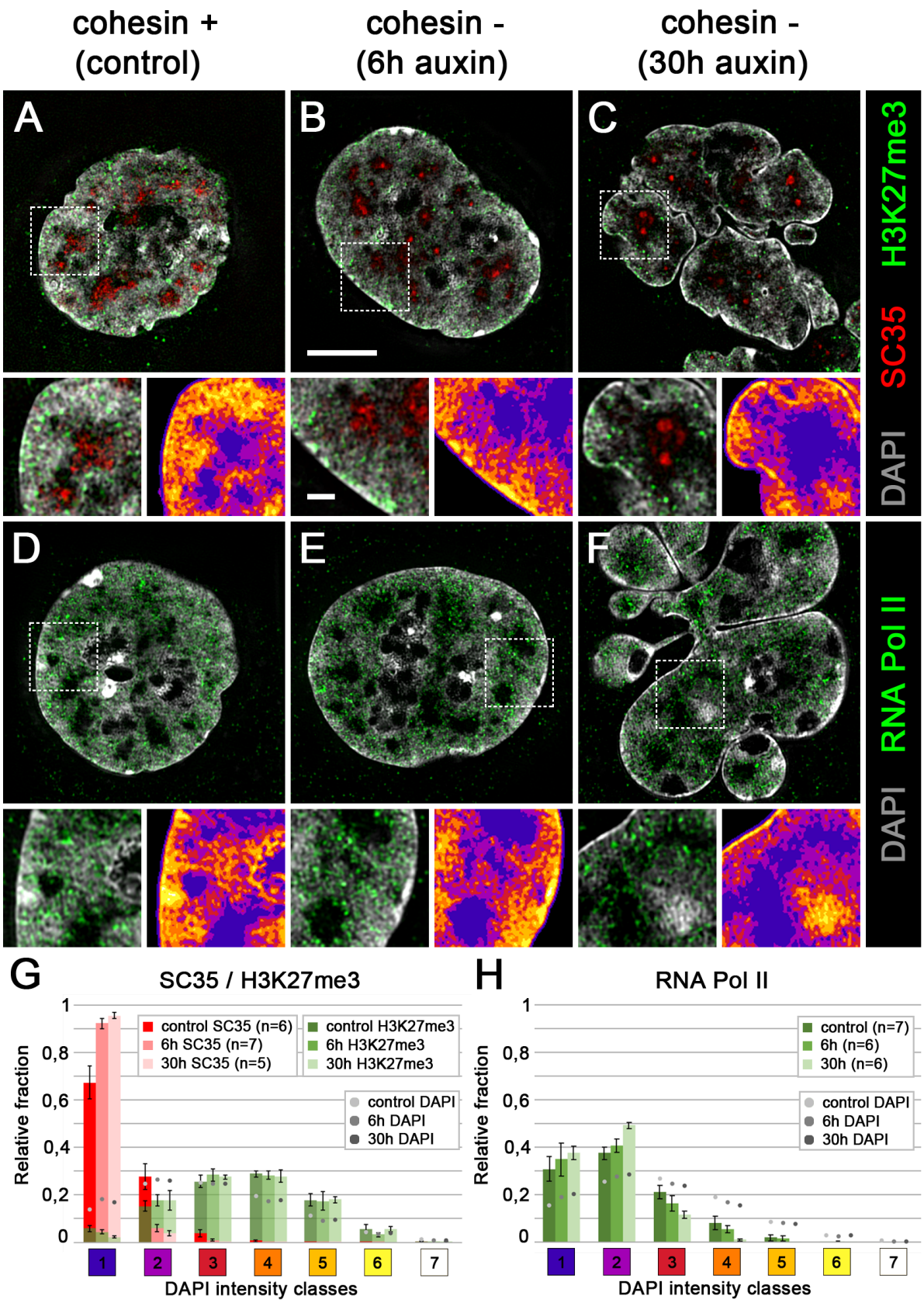

Fig. 4: Maintenance of the 3D topography in cohesin depleted nuclei for nuclear markers SC35, H3K27me3 and active RNA Pol II on chromatin compaction maps

(A-F) SIM optical mid-sections from whole 3D acquisitions of DAPI stained nuclei (gray) with representative zoomed magnifications also displayed as classified DAPI intensity heat maps. **(A-**

C) Immunostaining of SC35 (red) and H3K27me3 (green), **(D-F)** of active RNA Pol II with (A,D)=controls, (B,E) = 6h auxin treatment, (C,F) = postmitotic MLN after 30h auxin treatment. SC35 is mostly seen in class 1 reflecting the interchromatin compartment (IC), H3K27me3 is enriched in more compacted chromatin regions (classes 3-5). RNA Pol II shows a preferential localization at decondensed chromatin sites lining the IC in D-F**.** Scale bar: 5 µm in mid-sections; 1 µm in insets. **(G)** Relative signal distribution of SC35 (red) and H3K27me3 (green), **(H)** of active RNA Pol II (green) on DAPI intensity classes 1-7 (DAPI distribution is marked as gray dots). The different color shades denote controls, 6h auxin and 30h auxin treated cells. With exception for SC35 in controls and cohesin depleted nuclei marker distributions between controls and cohesin depleted nuclei do not show significant differences (for statistical tests and significance see Suppl_Table 1).

In situ Hi-C data indicate a consistent disappearance of chromatin loops in cohesin depleted pre- and postmitotic nuclei but maintenance of A and B compartments

In situ Hi-C confirmed the disappearance of loop domains previously described in cohesin depleted premitotic cells [18, 20] also in postmitotic cell cultures, which were treated with auxin for 28h before fixation (Fig. 5A). In these cultures, most cells carried MLN (compare suppl_Fig.3). A and B compartments are reconstituted in these postmitotic MLN (Fig. 5B). A heightened compartmentalization was noted in particular in B-type chromatin of MLN, as previously described for premitotic cohesin depleted cells [18]. Even in our low depth data from 28h auxin treated postmitotic MLN cells, the strengthened interactions between this B-type subcompartment could be readily observed (Fig. 5C,lower right panel). While the functional identity or significance of this particular B-type subcompartment remains unknown, by k-means clustering of histone modification data for HCT116-RAD21-mAC cells [18], we were able to identify a histone modification cluster (consisting of depletion of both activating marks like H3K36me3 and H3K27Ac and repressive marks such as H3K27me3 and H3K9me3, but a mild enrichment of H3K79me2) that corresponded to the positions of this particular B-type subcompartment (Fig 5D).

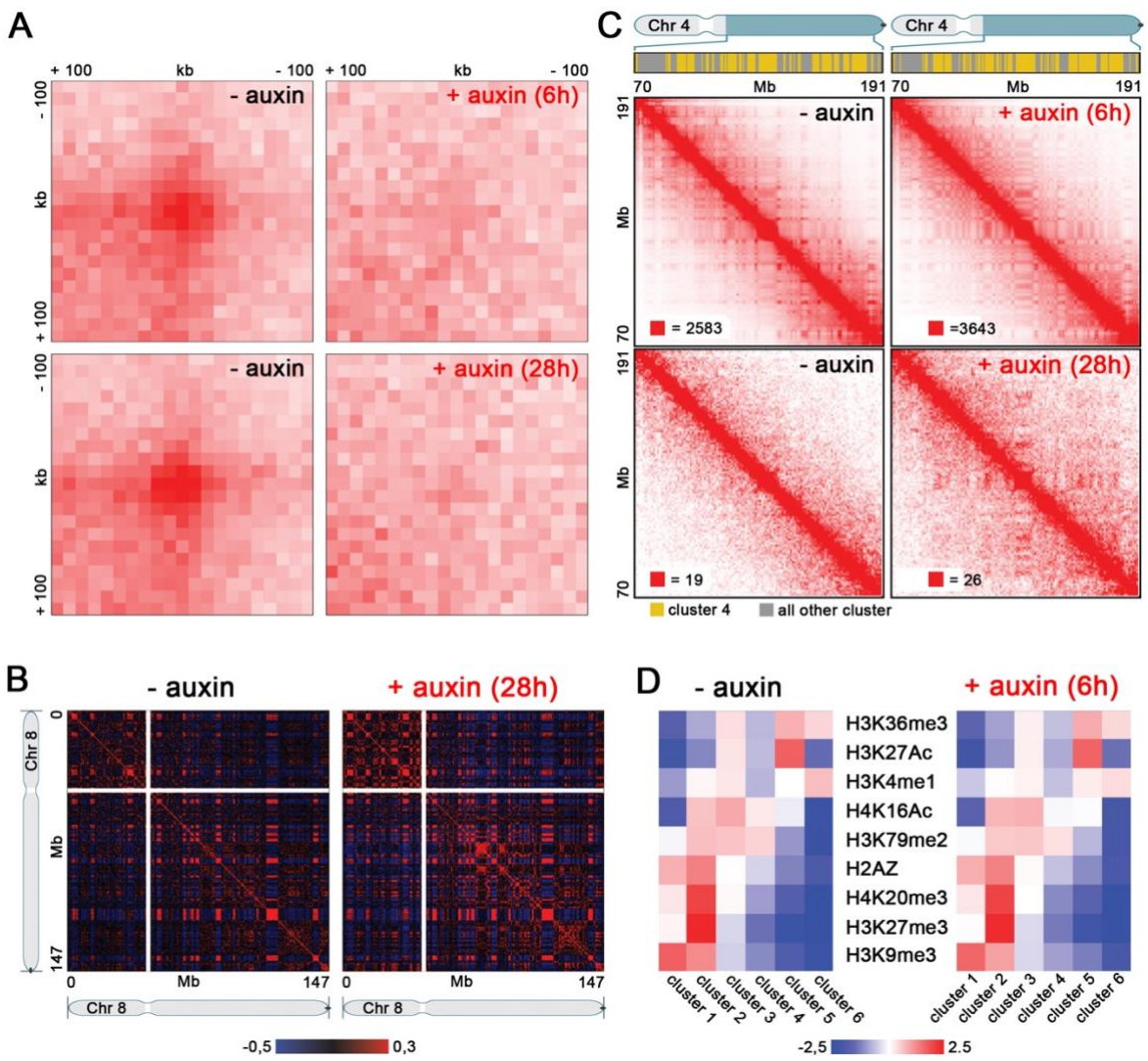

Fig. 5: Hi-C data indicate elimination of chromatin loops, but maintenance of A and B compartments in cohesin depleted pre- and postmitotic cells

(A) Aggregate peak analysis **(**APA) plots using loops identified in HCT116-RAD21-mAC cells [18] before and after 6h of auxin treatment (top) or before and after 28h of auxin treatment (bottom). The plot displays the total number of contacts that lie within the entire putative peak set at the center of the matrix. Loop strength is indicated by the extent of focal enrichment at the center of the plot. **(B)** Pearson's correlation maps at 500 kb resolution for chromosome 8 before (left) and after (right) 28h of auxin treatment. The plaid pattern in the Pearson's map, indicating compartmentalization, is preserved in cohesin depleted nuclei even after 28h of auxin treatment. **(C)** Contact matrices for chromosome 4 between 70 Mb and 191 Mb at 500 kb resolution before (left) and after (right) cohesin depletion. The 6h cohesin depletion time is shown on top, and 28h depletion time on the bottom. Interactions for loci in cluster 4 (annotated in yellow on top tracks) are strengthened after both 6h or 28h of cohesin depletion. All loci belonging to clusters other than cluster 4 are annotated in gray in the top track. **(D)** Clustering of histone modifications at 25 kb resolution into six clusters reveals consistent clusters of histone modification before and after cohesin depletion. For each cluster, the average log2-fold enrichment for each histone modification over all loci in that cluster is shown.

Same replication timing for cohesin depleted and non-depleted control cells seen by Hi-C and Repli-Seq data

Using Repli-Seq and Hi-C analysis replication timing was measured by the ratio of early to late replicating DNA and was found preserved upon cohesin depletion (Suppl_Fig. 5A,B). Additionally, the tight relationship between genome A/B compartmentalization and replication timing was similarly maintained in the absence of cohesin (Suppl_Fig. 5C).

Persistence of typical S-phase stage replication patterns after cohesin depletion and their restoration in postmitotic MLN

The temporal order of DNA replication occurring at distinct replication sites as replication foci is highly coupled with genome architecture, resulting in typical patterns for early, mid and late replication timing [39]. These replication sites persist as stable chromatin units (replication domains, RDs) throughout interphase and during subsequent cell cycles [40-43] and were chosen in our study as reference structures for CDs (see Discussion). Replicating DNA was visualized by pulse replication labeling (RL), using an approach where fluorophore-conjugated dUTPs are incorporated by a short scratch of S-phase cells [42, 44]. RDs could then be visualized through the remaining and the next cell cycle without further detection steps. Images were acquired by 3D-SIM.

RD patterns were recorded in cells with the following culture conditions: Control cultures were fixed 6h after RL (Fig. 6A). Cultures prepared for cohesin depletion were further grown after RL for 1h under normal medium conditions and then exposed to auxin for 6h (Fig. 6B,C) or 30h respectively (Fig. 6D), before fixation. Both, controls and auxin-treated cells revealed typical RD patterns for all S-phase stages. Fig. 6C shows a labeled nucleus that has entered mitosis. Our observations demonstrate that a given RD pattern not only persists during the subsequent interphase and along mitotic chromosomes (Fig. 6B,C) but can also be fully reconstituted after mitosis in MLN (Fig. 6D).

Moreover we showed that *de novo* DNA synthesis with the formation of typical replication patterns still occurs in cohesin depleted postmitotic MLN. Fig. 6E shows examples

361 where RL was performed under continuous auxin treatment in cells that were kept in auxin for

362 30h prior to RL.

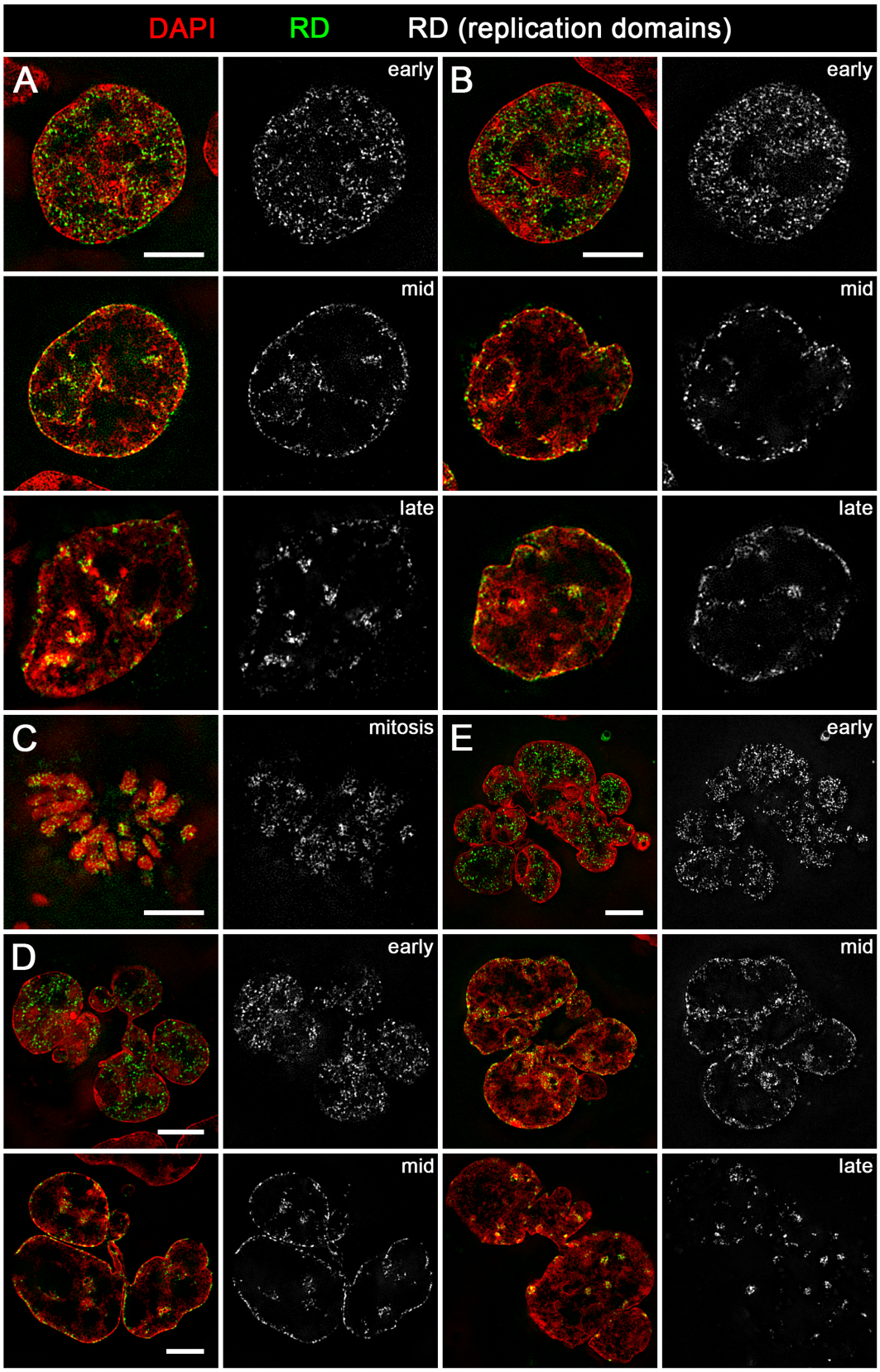

363

364 **Fig. 6: Maintenance, postmitotic re-establishment and de novo formation of typical**

365 **replication patterns after cohesin depletion**

(A-E) Representative SIM sections of DAPI stained nuclei (red) with replication domains (RDs, green in overlay images) in different cell cycle stages. Respective RDs are in addition separately shown in gray. **(A)** Control nuclei fixed 6h after replication labeling (RL) delineating the typical patterns for early, mid and late replication. **(B)** Maintenance of typical replication patterns in cohesin depleted nuclei. For complete cohesin depletion nuclei were incubated for 6h in auxin after replication labeling performed in normal medium conditions. **(C)** Mitosis with RDs emerging from a replication labeled nucleus under conditions as described in (B). **(D)** Replication patterns in a postmitotic multilobulated nucleus (MLN). RL was performed in normal medium conditions and cells subsequently treated with auxin for 30h. Re-established RDs form typical early and mid-to-late replication patterns in individual lobuli. **(E)** *De novo* DNA synthesis with formation of typical replication patterns in MLN. Cells were treated with auxin for 30h prior to replication labeling under continuous auxin conditions. Scale bar: 5 µm.

Individual replication domains (RDs) and DNA halo induced chromatin loops are enlarged in cohesin depleted cells

Finally, we tested whether cohesin depletion following RL during early S-phase results in numerical and/or structural changes of individual RDs (Fig. 7). We compared numbers of segmented RDs plotted as the mean value of counts / nucleus (Fig. 7B) and the total volumes of all segmented RDs, plotted as the mean total RD volume / nucleus (Fig. 7C) between control nuclei grown for 6h after RL in normal medium conditions, premitotic nuclei grown for 6h in auxin after RL, and postmitotic MLN grown for 30h in auxin after RL. Both, total volumes and counts of segmented RDs were higher in cohesin depleted nuclei and slightly increased with the duration of auxin induced degradation of cohesin, hinting to chromatin relaxation at the level of individual RDs.

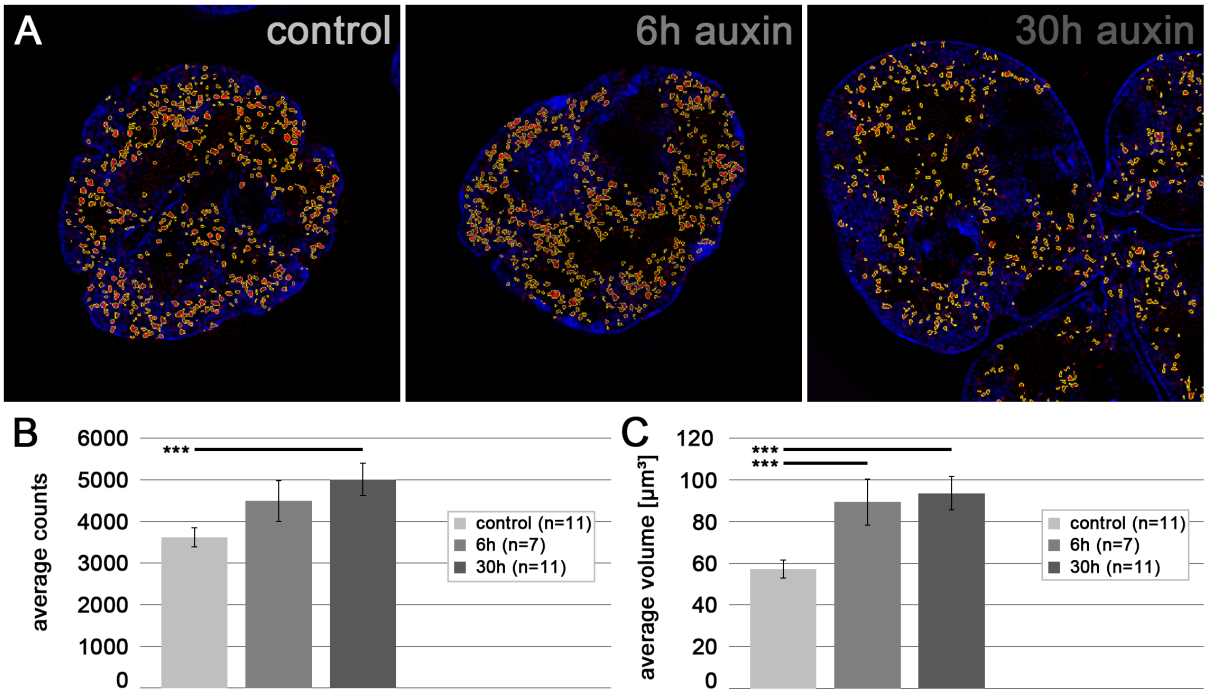

Fig. 7: Segmentation of individual replication domains established in early S-phase
(A) SIM optical mid-sections of DAPI stained nuclei (blue) from a control *(left)*, a 6h auxin treated nucleus *(mid)* and a 30h auxin treated MLN *(right)*. Replication labeling was performed prior to cohesin depletion. RDs are displayed in red with segmented borders lined in yellow. The lower density of RDs in the postmitotic MLN is clearly evident. **(B)** Average counts of segmented RDs plotted as the mean value of object counts / nucleus in each series. **(C)** Volumes of segmented RDs plotted as the mean total volume of RDs/nucleus in each series. Significance ($p<0.05$) between series indicated by asterisks. Scale bar: 4 µm

An effect of cohesin depletion on RD structure was supported by a DNA halo approach, a technique to investigate changes in chromatin organization at the level of DNA loops [45]. Histone extraction in interphase nuclei by high-salt incubation triggers the extrusion of chromatin loops from a densely stained central chromatin core thus providing a measure of their size. DAPI stained nuclei of cohesin depleted cells (6h auxin treatment) exhibited halos that were significantly larger and more variable in shape in comparison to the defined and compacted halos of control cells (Suppl_Fig. 6).

Discussion

Perturbed mitoses with formation of a single postmitotic multilobulated nucleus (MLN) in cohesin depleted cells

Our Repli-Seq data and live cell observations confirm an undisturbed cell cycle progress of cohesin depleted cells towards mitosis [28] and a disturbed course of mitotic progress [46]. In addition our time lapse observations reveal a so far unreported arrest of telophase in conjunction with a lack of cytokinesis, resulting in a single postmitotic cell harboring one MLN. Several factors may contribute to this outcome: cohesin loss was previously shown to prompt a defect of centrosome duplication and spindle pole integrity, as well as a compromised cohesin-mediated kinetochore-microtubule attachment [46] (reviewed in [1, 2]). Notably, in vertebrates cohesin is loaded onto DNA already in telophase [1, 5], which may be relevant for correct cytokinesis and daughter cell formation. Loss of cohesin is, however, not mandatory for the formation of MLN. MLN are found in cells with a mutant CTD Thr4-phosphorylation in a mitosis-specific form of RNA Pol II [47]. Multilobulation also arises in terminally differentiated granulocytes [48] and in tumor cells with extensive chromosomal rearrangements, such as Hodgkin lymphoma associated Reed-Sternberg cells [49]. Our observation of MLN as the mitotic outcome in ~2% of HCT116-RAD21-mAC control cells exemplifies the spontaneous occurrence of MLN in a near-diploid tumor cell line. Overall, the complex interactions of factors promoting MLN are still poorly understood [50, 51].

Maintenance of principle features of higher order chromatin architecture in cohesin depleted nuclei in line with the ANC-INC model

Hallmarks of the ANC-INC model (reviewed in [23-25], see Introduction) were retained in cohesin depleted pre- and postmitotic cell nuclei. These hallmarks include the preservation of chromosome territories (CTs), chromatin domain clusters (CDCs) structurally organized by different compaction levels, an interchromatin (IC) channel system and the maintenance of an active compartment (ANC), represented by markers for transcriptional competence (here active RNA Pol II and splicing speckles) and a co-aligned inactive compartment (INC) with

repressed chromatin (H3K27me3).

We also examine replication domains (RDs). RDs defined by genome-wide Repli-Seq analyses are often considered to correspond to TADs mapped by Hi-C methods [27, 52] and as molecular equivalents of replication foci / domains observed by microscopic methods [53]. Yet, a direct comparison of these structures is a delicate issue since neither RDs nor TADs are strictly defined: microscopically observable replication sites were initially reported in rat fibroblast nuclei with an average DNA content of ~1 Mb [54]. Later studies with conventional and super-resolution microscopy [40, 44, 55] showed that RDs with an average DNA content of 400–800 kb [56] can be optically resolved down to a few single replicons (150–200 kb) clustered per replication site. Similarly, the definition of TADs with a size range of ~0.1-1Mb (and further grouping into subTADs and metaTADs) has remained somewhat fuzzy, likely due to their dynamic behavior [57], differences of evaluation mode and interpretation [58, 59].

A recent review rejected the above hierarchy of metaTADs, TADs, and subTADs, and instead argued for a very different classification of contact domains into two types [60]: compartmental domains which originate due to the co-segregation of chromatin intervals with similar marks, and loop domains, which emerge from cohesin extrusion.

Critically, in our study, we report the maintenance of replication domains (RDs) in cohesin depleted nuclei over mitosis with re-formation of typical patterns for all S-phase stages in postmitotic MLN. Thus, replication domains remain despite the loss of all loop domains (whether classified as TADs, subTADs, metaTADs, etc). Instead, we find that the boundaries of replication domains align with the boundaries of compartmental domains. Thus, our work is consistent with the view that there are two types of domains. Compartmental domains, which do not depend on cohesin extrusion, correspond closely to replication domains. By contrast, loop domains, which result from cohesin extrusion, do not correspond to the boundaries of replication domains.

Disappearance of loop domains and concomitant persistence of functional higher order chromatin arrangements underpins different mechanisms for their structural organization

The disappearance of chromatin loops as basic chromatin folding structures demonstrated by Hi-C experiments may lead to the expectation of a profound effect on the global higher order chromatin organization, like a house of cards falling together when a basal card is removed. Apparently, this is not the case as has been previously shown by the maintenance and even strengthening of compartmentalization into A and B domains after cohesin depletion [18, 20]. In the present study the persistence of compartment domains was also demonstrated for cultures highly enriched with postmitotic MLN.

Chromatin loop domains are formed by means of an extrusion mechanism where by the gradual expansion of a loop through a cohesin ring two opposite CTCF sites are tethered together and anchored at CTCF/cohesin binding sites (reviewed in [6, 61-64]). These anchor sites manifest as bright peaks in Hi-C maps. Based on cohesin depletion experiments this loop extrusion mechanism was shown to be cohesin dependent ([18, 20, 21] and this study). Elimination of cohesin dependent chromatin loop domains visualized in Hi-C maps by the respective disappearance of squares of enhanced contact frequencies does, however, not necessarily reflect a complete loss of chromatin loops. An effect of cohesin depletion on chromatin decompaction / relaxation with a modest increase of RD diameters as found in our present study may already result in a major decrease of 3D contact frequencies and contribute to the failure to detect loop domains. Our observation that replication foci become physically larger after cohesin depletion also suggests cohesin dependent extrusion may play a role in the physical compaction of replicating chromatin. This is consistent with a model where cohesin extrusion tends to compact intervals of replicating chromatin, but where their genomic boundaries are associated with compartmentalization [29].

Moreover, cohesin rings as chromatin loop anchors may in part be replaced after cohesin depletion by other factors with less defined anchor points (reviewed in [6, 7, 63]). The entrance of cells into mitosis provides a case in point for a structural change of chromatin loop organization which prompts a loss of the Hi-C plaid or check-board pattern in mitotic chromosomes [65]: upon entering mitosis, cohesin is lost from chromosome arms (reviewed in [1]) and helically arranged nested loop arrays are formed by condensins I and II. The organization of chromatids in mitosis can be described as a linearly organized, longitudinally

compressed array of consecutive chromatin loops [66]. Notwithstanding this major change of chromatin loop organization between interphase and mitosis, major features of higher order chromatin organization persist and are transmitted from one cell cycle to the next [67, 68]. Chromatin loop clusters attributed to distinct CDs during interphase continue to be present in close spatial arrangements along mitotic chromosomes which allows the rapid re-establishment of loops, domains and compartments early in G1.

Cohesin-independent maintenance of Hi-C detectable A and B compartments was reported in several studies (reviewed in [22]). In line with only minor effects of cohesin depletion on gene expression [18], the present study underpins that mechanisms that direct the maintenance of individual RDs and their spatio-temporal order, as well as the spatial arrangement of higher order chromatin organization in the context of the ANC-INC model are also independent of cohesin and sufficient to instruct accurate reformation of these structures upon exit from mitosis into a subsequent cell cycle in the absence of cohesin. We argue that RDs correspond with compartment domains in line with [29] where discrete cis-regulatory elements which orchestrate domain-wide replication timing, A/B compartmentalization and loop architecture, were identified.

An integrated view of the functional nuclear landscape based on Hi-C and microscopic data

Although microscopically derived distance maps were reported in excellent agreement with Hi-C maps [69], Hi-C and microscopy yield different views on the nuclear landscape and unexplored gaps between findings obtained with these approaches have to be closed. Hi-C has made possible the genome wide identification of the spatial proximity of DNA segments in cis and trans [12-14, 70] and genome wide data on chromatin modifications and architectural proteins mapped along the DNA can be easily integrated into the resulting architectural landscape. However, as a method based on 3D DNA-DNA contact frequencies Hi-C lacks the power to identify the system of IC-channels and the lining PR. These features have been demonstrated consistently in many cell types and species with super-resolved microscopy [24, 25]. The relationship of compartments A and B identified by Hi-C with the co-aligned

compartments described by the ANC-INC model has not yet been clarified. Some studies traced genomic features within a range of few Mb with a combination of super-resolved microscopy and Hi-C [71, 72]. Using stochastic optical reconstruction microscopy, Bintu et al. [71] demonstrated domain-boundary-like structures in single cohesin depleted nuclei. Loss of cohesin, however, abolished preferential boundary sites with a corresponding loss of loop domains detectable by Hi-C at the population-average level in cohesin depleted cells.

Furthermore, Hi-C is not an appropriate method to measure absolute chromatin compaction. Simply put, Hi-C does not measure absolute contact frequency, and 3D reconstructions of higher order chromatin organization from Hi-C data have sometimes been used to argue for relatively open and accessible lariat-like chromatin loop structures [69, 73-76]. In contrast, recent studies using advanced microscopic strategies have suggested nucleosome clusters (NCs) as basic entities of chromatin organization beyond the nucleosome level [77-79]. Chromatin loops built from NCs imply more compacted and less accessible CDs with profound consequences for their accessibility for macromolecules (see below). Cartoons of 3D TAD structures [69, 73-76] suggest an unconstrained access of individual macromolecules, such as transcription factors, into the interior and also a constrained accessibility of macromolecular complexes. In contrast, we and others [80] consider the possibility that the accessibility of CDs may be impeded to an extent that the diffusion of individual macromolecules is constrained, and macromolecular complexes are fully excluded. We postulate that this basic organization is maintained in cohesin depleted nuclei.

Outlook

The polymer melt model of the CD structure proposed by Maeshima and colleagues [81] argues for dense packaging of ~10 nm thick chromatin fibers in the interior of CDs. Based on Monte Carlo simulations Maeshima et al. [80] proposed that nucleosome densities >0.3 to 0.5 mM, corresponding to DNA densities of ~40 – 60 Mb/μm^3, result in an accessibility barrier for molecule complexes with diameters >20 – 25 nm. Estimates of DNA densities based on super-resolved microscopy of CDs in various human and mouse cell nuclei indicate a range in the order of 5 - 200 Mb/μm^3 (C. Cremer, unpublished data). These estimates argue for an

554 exclusion of macromolecular complexes from the interior of CDs with higher compaction levels
555 and thus favor models proposing that macromolecular complexes involved in transcription and
556 other important nuclear functions act at the periphery of CDs [24, 25, 80, 82]. The implications
557 of this model for the mobility of CDs and functional DNA targets have remained elusive. In line
558 with current views of chromatin organization based on the formation of chromatin droplets with
559 distinct chromatin states [60], a recent Hi-C based genome-wide model depicts contact
560 domains and TADs as separated chromatin balls [83]. We have postulated that the IC may
561 provide preferred routes for imported transcription factors to their target sites, for the
562 intranuclear passage of regulatory RNAs to remote functional sites, and for export routes of
563 mRNPs towards nuclear pores [25]. In order to test this hypothesis, it is necessary to explore
564 the space-time compaction and accessibility of CDs. Super-resolved fluorescence microscopy,
565 including single molecule localization microscopy (SMLM) and stochastic optical
566 reconstruction microscopy (STORM), may become the methods of choice to measure absolute
567 differences of DNA/chromatin compaction with spatial resolution at the nanometer scale [79,
568 84, 85], whereas chromatin accessibility can be probed indirectly with methods that allow to
569 measure molecular diffusion rates [86-89].
570

571 **Materials & Methods**

572 *Cells and culture conditions*

573 HCT116-RAD21-mAID-mClover cells (referred to as HCT116-RAD21-mAC cells in the
574 manuscript) were generated and kindly provided by the Kanemaki lab (Mishima Shizuoka,
575 Japan; [16]). For a detailed description see Suppl_Fig. 1. Cells were cultured in McCoy's 5A
576 medium supplemented with 10% FBS, 2 mM L-glutamine, 100 U/ml penicillin, and 100 µg/ml
577 streptomycin at 37°C in 5% CO_2.
578

579 *Auxin induced RAD21 proteolysis*

580 Degradation of the AID-tagged RAD21 was induced by addition of auxin (indole-3-acetic acid;
581 IAA, Sigma Aldrich) to the medium at a final concentration of 500 µM (auxin stock solution 2
582 M in DMSO). In long term cultures fresh auxin-medium was added after 20-24h.
583

584 *Immunodetection*

Cells were grown on high precision coverslips (Roth, LH22.1, #1.5) to 80% confluency and washed two times in PBS before fixing them in 2% formalin/PBS for 10 min. After a stepwise formalin exchange with PBS/Tween 0.02%, cells were permeabilized with 0.5% Triton X-100/PBST for 10 min and then incubated in 2% BSA/PBST as blocking solution for 1h to minimize non-specific antibody binding. For immunodetection, primary and secondary antibodies were diluted in blocking solution and incubated each for 1h in a dark humified chamber to prevent drying and fluorescence fading. Primary antibodies against cohesin subunits RAD21, SMC1, SMC3 (Abcam), all raised in rabbit, were detected with Cy3-conjugated goat anti rabbit antibodies (Abcam). Primary antibodies against SC35 (Sigma), RNA Pol II (Abcam) and H3K27me3 (Active Motif) were detected with either donkey anti mouse Alexa 488 (Life technologies) or donkey anti rabbit Alexa 594 (Life technologies). A postfixation step in 4% formalin/PBS helped to stabilize bound antibodies. Cells were counterstained in 1 µg/ml DAPI, mounted in antifade mounting medium Vectashield (Vector Laboratories) and sealed with nail varnish (for details see [90]).

Replication pulse labeling

1. replication scratch labeling: Cells cultivated on high precision coverslips (thickness 0.170 mm) grown to 50-80% confluency were transferred into a dry empty tissue dish after draining off excess medium. 30 µl of the prewarmed labeling solution (20 µM Cy3-dUTP (homemade) or Alexa 594-5-dUTP (Life technologies)) was evenly distributed over the coverslip. With the tip of a hypodermic needle parallel scratches at distances of ~100 µm were quickly applied to the cell layer. Cells were incubated for 1 min in the incubator, then a few ml of pre-warmed medium was added to the dish. After 30 min medium was exchanged to remove non-incorporated nucleotides (for details see [42, 91]). Avoidance of any chemical treatments preserves the RAD21-mClover fluorescence after labeling and was therefore used for all RL experiments with exception for the labeling experiment shown in Fig. 6E.

2. Incorporation of 5-Ethynyl-dU (EdU) and detection by „click chemistry“

This approach was used for RL in MLN since these cells are prone to detachment upon scratching (compare Fig. 6E) taking the degradation of the protein-tagged RAD21-mClover fluorescence caused by the acidic reaction [92]. EdU was added at a final concentration of 10 µM to the medium for 15min. Incorporated EdU was detected according to manufactures instructions (baseclick) by a Cu(I) catalyzed cycloaddition reaction that covalently attaches a fluorescent dye containing a reactive azide group to the ethynyl-group of the nucleotide [93]. For visualization of RDs, the dye 6-FAM-Azide (baseclick) at a final concentration of 20 µM was used.

After either labeling approach cells were washed in 1xPBS and fixed with 4% formaldehyde / PBS for 10 min. After a stepwise exchange with PBST, cells were permeabilized with 0.5%

Triton X-100/PBS/Tween 0.02% for 10 min and washed again in 1xPBS. Cells were counterstained in 1 µg/ml DAPI and mounted in antifade mounting medium Vectashield (Vector Laboratories); for details see [90]).

HI-C in situ analysis of untreated and auxin treated cells

HCT-116-RAD21-mAC cells were plated in 6 well plates with either complete media, or complete media with 500uM auxin (IAA) for 6 hours (as in [22]) or 28 hours (to enrich for post-mitotic cells with multilobulated nuclei). Cells were crosslinked with 1% formaldehyde directly on the plate for 10 minutes and then quenched with glycine. The crosslinked cells were then scraped off and *in situ* Hi-C was performed as in [14]. In brief, cells were permeabilized with nuclei intact, the DNA was digested overnight with MboI, the 5'-overhangs were filled in while incorporating bio-dUTP, and the resulting blunt end fragments were ligated together. Crosslinks were then reversed overnight, the DNA was sheared to 300-500bp for Illumina sequencing, biotinylated ligation junctions were captured using streptavidin beads and then prepped for Illumina sequencing. We prepared 3 libraries (two biological replicates) each for each time point (untreated 6 hours, treated 6 hours, untreated 28 hours, treated 28 hours). All Hi-C data was processed using Juicer [94, 95]. The data was aligned against the hg19 reference genome. All contact matrices used for further analysis were KR-normalized with Juicer. Comparison of compartment strengthening to histone modification clusters was done as in [22]. Histone modification data for 9 marks (H3K36me3, H3K27Ac, H3K4me1, H4K16Ac, H3K79me2, H2AZ, H4K20me3, H3K27me3, H3K9me3) generated from untreated and 6-hour treated cells in [22] was grouped into 6 clusters using k-means clustering. For the k-means clustering, the histone modification data was first converted into a z-score value for each mark in order to account for differences in the dynamic range between marks.

Repli-Seq of untreated or auxin-treated cells

HCT116-RAD21-mAC cells were synchronized in G1 with lovastatin as previously described [96]. Briefly, cells were incubated with 20 µM Lovastatin (Mevinolin) (LKT Laboratories M1687) for 24 hours to synchronize in G1. 500 µM auxin or DMSO was added 6 hours before release from lovastatin block. To release from G1 block, lovastatin was washed away with 3 washes of PBS and warm media plus 2 mM Mevalonic acid (Sigma-Aldrich M4667) and 500 µM Auxin or DMSO. Cells were released for 10, 14, 18, and 22 hours. 2 hours before the time point 100 µM BrdU was added to label nascent replication. After fixation, equal numbers of cells from each release time point were pooled together for early/late repli-seq processing [97]. Repli-Seq data was processed as described in [97]. In brief, data was aligned to the hg19 reference genome using bowtie2, deduplicated with samtools, and the log-2 ratio between early and late timepoints was calculated.

661
662
663 *3D DNA-FISH*
664 Hapten - or directly labeled chromosome painting probes delineating human chromosomes 4-
665 (BIO), 12-(DIG) and 19-Cy3, generated from flow sorted chromosomes as previously
666 described in detail [30] were kindly provided by Stefan Müller (LMU). 30 ng of each labeled
667 probe and a 20-fold excess of COT-1 DNA was used per 1 µl hybridization mix (50%
668 formamide/ 2xSSC/ 10% dextran sulfate).
669 Cells were washed in 1xPBS and fixed with 4% formaldehyde/PBS for 10 min. After a stepwise
670 exchange with 0.5% Triton X-100/PBS, cells were permeabilized with 0.5% Triton X-100/PBS
671 for 10 min, washed in 1xPBS. Further pretreatment steps included incubation in 20% glycerol
672 (1h), several freezing/thawing steps in liquid N_2, and incubation in 0.1 N HCl (5 min). Cells
673 were stored in 50% formamide/2xSSC overnight. After simultaneous denaturation of probe and
674 cells (2 min at 76°C), hybridization was performed at 37°C for 48h. After stringent washing in
675 0.1xSSC at 60°C, biotin was detected by streptavidin-Alexa 488 and DIG by a mouse-anti-DIG
676 antibody conjugated to Cy5. Cells were counterstained in 1 µg/ml DAPI, mounted in antifade
677 mounting medium Vectashield (Vector Laboratories) and sealed with nail varnish (for details
678 see [30]).
679
680 *DNA halo preparation*
681 HCT116-RAD21-mAC cells were incubated for 6h in 500 µM auxin for cohesin depletion. DNA
682 halo preparation was largely performed according to [98]. After washing the cells in 1xPBS
683 they were incubated for 10 min in a buffer at 4°C containing 10 mM Tris pH 8, 3 mM $MgCl_2$,
684 0.1 M NaCl, 0.3 M sucrose, protease inhibitors (freshly added to the buffer prior to use) 1 µM
685 pepstatin A, 10 µM E64, 1 mM AEBSF and 0.5% Nonidet P40. All the following procedures
686 were performed at room temperature. Subsequently DNA was stained for 4 min with 2 µg/ml
687 DAPI. After 1 min in a second extraction buffer (25 mM Tris pH 8, 0.5 M NaCl, 0.2 mM $MgCl_2$;
688 protease inhibitors as in nuclei buffer and 1 mM PMSF were added fresh prior to use), cells
689 were incubated 4 min in halo buffer (10 mM Tris pH 8, 2 M NaCl, 10 mM EDTA; protease
690 inhibitors as in nuclei buffer and 1 mM DTT were added fresh prior to use). Eventually cells
691 were washed 1 min each in two washing buffers (25 mM Tris pH 8, 0.2 mM $MgCl_2$; the first
692 buffer with and the second without 0.2 M NaCl). After 10 min fixation in 4% formaldehyde/PBS,
693 cells were washed twice in 1xPBS, mounted on slides with Vectashield and sealed with nail
694 varnish.
695 Nuclear scaffolds and the faded DNA halos were imaged at a widefield microscope (Zeiss
696 Axioplan 2, 100x/1.30 NA Plan-Neofluar Oil Ph3 objective; Axiovision softare; AxioCam mRM
697 camera). Both the total area (At) and the scaffold area (As) of each cell were manually
698 segmented using the software Fiji and the DNA halo area (Ah) calculated as a subtraction of

the two (Ah = At – As). The DNA halo radius was subsequently derived with the formula R = √(Ah/π). Four biological replicates were prepared and measured. For generation of plots and statistical analysis (Wilcoxon test) the software RStudio was used.

Confocal fluorescence microscopy

Confocal images were collected using a Leica SP8 confocal microscope equipped with a 405nm excitation laser and a white light laser in combination with an acousto-optical beam splitter (AOBS) which allows tunable filtering of excitation from 470 to 670 nm and freely programmable emission detection. The used confocal system has three different detectors, one photomultiplier tube (PMT) and two hybrid photodetectors (HyD). The microscope was controlled by software from Leica (Leica Application Suite X, ver. 3.5.2.18963). For excitation of DAPI, the 405 nm laser was used. For excitation of Alexa488, Cy3, STAR635P and Cy5, the white light laser was set to 499, 554, 633 and 649 nm, respectively. The emission signal of DAPI was collected by the PMT (412-512 nm), the emission signals of Alexa488 (506-558 nm), Cy3 (561-661 nm), STAR635P (640-750 nm) and Cy5 (656-780 nm) were collected by the two HyD detectors. Images were acquired with 42 nm pixel steps, 102 µs pixel dwell time and 2-fold line accumulation using a Leica HC PL APO 63x/1.30 NA Glycerol immersion objective. The frame size was 37 x 37 µm and the scan speed was 700 Hz. The size of the confocal pinhole was 1 A.U. Confocal image z-stacks were acquired with a step size of 330 nm.

Live cell microscopy for long term observations

For live cell imaging, cells were plated on poly-L-Lysine-coated glass bottom 2-well imaging slides (ibidi), allowing to image control and auxin-treated conditions in parallel. For DNA staining cells were grown in media containing 500 nM SiR-DNA (Spirochrome) for 1h before imaging. Timelapse acquisitions were carried out on a Nikon TiE microscope equipped with a Yokogawa CSU-W1 spinning disk confocal unit (50 µm pinhole size), an Andor Borealis illumination unit, Andor ALC600 laser beam combiner (405 nm / 488 nm / 561 nm / 640 nm), and Andor IXON 888 Ultra EMCCD camera. The microscope was controlled by software from Nikon (NIS Elements, ver. 5.02.00). Cells were imaged in an environmental chamber maintained at 37°C with 5% CO2 (Oko Labs), using a Nikon PlanApo 60x/1.49 NA oil immersion objective and a Perfect Focus System (Nikon). Images were recorded every 15 min for 21h as z-stacks with two planes and a step size of 6 µm, unbinned and with a pixel size of 217 nm. For excitation of mClover and SiR-DNA, the 488 and 640 nm laser lines were used, respectively. Fiji software (ImageJ 1.51j) [99] was used to analyze images.

Semi-automatic quantitative evaluation of multilobulated nuclei (MLN) / mitoses

Image acquisitions were carried out on the Nikon spinning disk system described above. Using a Nikon PlanApo 100x/1.45 NA oil immersion objective tiled images (3x3 with 5% overlap and 131 nm pixel size) were acquired for each condition to increase the number of cells per field of view. Confocal image z-stacks were acquired in two planes with a step size of 6 µm in order to encompass cells, in particular mitotic cells, in different plane levels. DAPI and mClover were excited with 405 or 488 nm laser lines, respectively. All nuclei from each image (average 280 nuclei per image frame) were classified visually into morphologically normal nuclei, mitoses and multilobulated nuclei (MLN). In auxin treated cells nuclei with persistent RAD21-mClover fluorescence (~2%) were excluded.

Structured illumination microscopy (SIM)

Super-resolution structured illumination imaging was performed on a DeltaVision OMX V3 system (Applied Precision Imaging/GE Healthcare) equipped with a 100x/1.4 NA UPlan S Apo oil immersion objective (Olympus), Cascade II:512 EMCCD cameras (Photometrics) and 405, 488 and 593 nm lasers (for detailed description see [100]). For sample acquisition oil with a refractive index of RI=1.512 was used. 3D image stacks were acquired with 15 raw images per plane (5 phases, 3 angles) and an axial distance of 125 nm and then computationally reconstructed (Wiener filter setting of 0.002, channel specific optical transfer functions (OTFs)) and color shift corrected using the SoftWoRx software (Applied Precision Imaging/GE Healthcare). After establishing 32-bit composite tiff stacks with a custom-made macro in Fiji/ImageJ2 (http://rsb.info.nih.gov/ij/), the data were subsequently aligned again to get a higher alignment precision. These images were then used for measurements in the Volocity software (Perkin Elmer).

Segmentation and quantification of replication domain (RD) signals

Aligned 3D SIM image stacks were used as RGB for object counting and volume measurements in the Volocity software. For each series between n=7 and n=11 nuclei were measured. The image stacks were separated in their respective channels and then structures were obtained and segmented separately. The segmentation of cohesin structures was performed with the following software commands: 1. “Find Objects” (Threshold using: Intensity, Lower: 32, Upper: 255), 2. “Separate Touching Objects” (Object size guide of 0,002 µm³) and 3. “Exclude Objects by Size”, excluding structures < 0,005 µm³. Exclusion of signals outside a selected nucleus was achieved by the commands “Intersect” and “Compartmentalize”. Segmentation of nuclei was realized by the following commands: 1. “Find Objects” (Threshold using: Intensity), 2. “Dilate”, 3. “Fill Holes in Objects” and 4. “Erode”. Measured values for volumes and object counts were plotted as histograms using bins for volume classes (0,01-0,4 µm³) and object counts within each bin. To compare different series, averaged values from all nuclei of a given series were used. To confirm statistically significance the Mann-Whitney test

was applied for both object counts and volumes. For comparability of the results, the same protocol was applied for all conditions

Chromatin compaction classification by 3D assessment of DAPI intensity classes

Nuclei voxels where identified automatically from the DAPI channel intensities using Gaussian filtering and automatic threshold determination. For chromatin quantification a 3D mask was generated in ImageJ to define the nuclear space considered for the segmentation of DAPI signals into seven classes with equal intensity variance by a previously described in house algorithm [34], available on request. Briefly, a hidden Markov random field model classification was used, combining a finite Gaussian mixture model with a spatial model (Potts model), implemented in the statistics software R [101, 102]. This approach allows threshold-independent signal intensity classification at the voxel level, based on the intensity of an individual voxel. Color or gray value heatmaps of the seven intensity classes in individual nuclei were performed in ImageJ.

Quantitative allocation of defined nuclear targets on 3D chromatin compaction classes

Individual voxels of fluorescent signals of the respective marker channels were segmented using a semi-automatic thresholding algorithm (using custom built scripts for the open-source statistical software R http://www.r-project.org, available on request). XYZ-coordinates of segmented voxels were mapped to the seven DNA intensity classes. The relative frequency of intensity weighted signals mapped on each DAPI intensity class was used to calculate the relative distribution of signals over chromatin classes. For each studied nucleus the total number of voxels counted for each intensity class and the total number of voxels identified for the respective fluorescent signals for SC35, RNA Pol II, H3K27me3 was set to 1. As an estimate of over/under representations (relative depletion/enrichment) of marker signals in the respective intensity classes, we calculated the difference between the percentage points obtained for the fraction of voxels for a given DAPI intensity class and the corresponding fraction of voxels calculated for the respective signals. Calculations were performed on single cell level and average values over all nuclei used for evaluation and plotting. For a detailed description see [34].

Acknowledgments

We thank Stefan Müller, University of Munich (LMU), for kindly providing labeled chromosome painting probes for 3D-FISH experiments and Irina Solovei, University of Munich (LMU), for generously providing antibodies, lab space and facilities to MC. We are most grateful to Toyoaki Natsume from the lab of Masato Kanemaki (Center of Frontier Research, National Institute of Genetics, Mishima, Shizuoka Japan) for providing HCT116-RAD21-mAC cells. KB

was supported by the International Max Plank Research School for Molecular Life Sciences (IMPRS-LS). Microscopic images were acquired at microscopes of the Center for Advanced Light Microscopy (CALM) at the LMU Munich.

References

1. Jeppsson K, Kanno T, Shirahige K, Sjogren C: **The maintenance of chromosome structure: positioning and functioning of SMC complexes.** *Nat Rev Mol Cell Biol* 2014, **15:**601-614.
2. Mehta GD, Kumar R, Srivastava S, Ghosh SK: **Cohesin: functions beyond sister chromatid cohesion.** *FEBS Lett* 2013, **587:**2299-2312.
3. Nasmyth K, Haering CH: **Cohesin: its roles and mechanisms.** *Annu Rev Genet* 2009, **43:**525-558.
4. Nishiyama T: **Cohesion and cohesin-dependent chromatin organization.** *Curr Opin Cell Biol* 2019, **58:**8-14.
5. Peters JM, Tedeschi A, Schmitz J: **The cohesin complex and its roles in chromosome biology.** *Genes Dev* 2008, **22:**3089-3114.
6. van Ruiten MS, Rowland BD: **SMC Complexes: Universal DNA Looping Machines with Distinct Regulators.** *Trends Genet* 2018, **34:**477-487.
7. Yuen KC, Gerton JL: **Taking cohesin and condensin in context.** *PLoS Genet* 2018, **14:**e1007118.
8. Parelho V, Hadjur S, Spivakov M, Leleu M, Sauer S, Gregson HC, Jarmuz A, Canzonetta C, Webster Z, Nesterova T, et al: **Cohesins functionally associate with CTCF on mammalian chromosome arms.** *Cell* 2008, **132:**422-433.
9. Wendt KS, Yoshida K, Itoh T, Bando M, Koch B, Schirghuber E, Tsutsumi S, Nagae G, Ishihara K, Mishiro T, et al: **Cohesin mediates transcriptional insulation by CCCTC-binding factor.** *Nature* 2008, **451:**796-801.
10. Rao SS, Huntley MH, Durand NC, Stamenova EK, Bochkov ID, Robinson JT, Sanborn AL, Machol I, Omer AD, Lander ES, Aiden EL: **A 3D map of the human genome at kilobase resolution reveals principles of chromatin looping.** *Cell* 2014, **159:**1665-1680.
11. Sofueva S, Yaffe E, Chan WC, Georgopoulou D, Vietri Rudan M, Mira-Bontenbal H, Pollard SM, Schroth GP, Tanay A, Hadjur S: **Cohesin-mediated interactions organize chromosomal domain architecture.** *EMBO J* 2013, **32:**3119-3129.
12. Dixon JR, Selvaraj S, Yue F, Kim A, Li Y, Shen Y, Hu M, Liu JS, Ren B: **Topological domains in mammalian genomes identified by analysis of chromatin interactions.** *Nature* 2012, **485:**376-380.
13. Lieberman-Aiden E, van Berkum NL, Williams L, Imakaev M, Ragoczy T, Telling A, Amit I, Lajoie BR, Sabo PJ, Dorschner MO, et al: **Comprehensive mapping of long-range interactions reveals folding principles of the human genome.** *Science* 2009, **326:**289-293.
14. Dixon JR, Gorkin DU, Ren B: **Chromatin Domains: The Unit of Chromosome Organization.** *Mol Cell* 2016, **62:**668-680.
15. Szabo Q, Jost D, Chang JM, Cattoni DI, Papadopoulos GL, Bonev B, Sexton T, Gurgo J, Jacquier C, Nollmann M, et al: **TADs are 3D structural units of higher-order chromosome organization in Drosophila.** *Sci Adv* 2018, **4:**eaar8082.
16. Natsume T, Kiyomitsu T, Saga Y, Kanemaki MT: **Rapid Protein Depletion in Human Cells by Auxin-Inducible Degron Tagging with Short Homology Donors.** *Cell Rep* 2016, **15:**210-218.
17. Natsume T, Kanemaki MT: **Conditional Degrons for Controlling Protein Expression at the Protein Level.** *Annu Rev Genet* 2017, **51:**83-102.
18. Rao SSP, Huang SC, Glenn St Hilaire B, Engreitz JM, Perez EM, Kieffer-Kwon KR, Sanborn AL, Johnstone SE, Bascom GD, Bochkov ID, et al: **Cohesin Loss Eliminates All Loop Domains.** *Cell* 2017, **171:**305-320 e324.
19. Gassler J, Brandao HB, Imakaev M, Flyamer IM, Ladstatter S, Bickmore WA, Peters JM, Mirny LA, Tachibana K: **A mechanism of cohesin-dependent loop extrusion organizes zygotic genome architecture.** *EMBO J* 2017, **36:**3600-3618.
20. Schwarzer W, Abdennur N, Goloborodko A, Pekowska A, Fudenberg G, Loe-Mie Y, Fonseca NA, Huber W, Haering CH, Mirny L, Spitz F: **Two independent modes of chromatin organization revealed by cohesin removal.** *Nature* 2017, **551:**51-56.
21. Wutz G, Varnai C, Nagasaka K, Cisneros DA, Stocsits RR, Tang W, Schoenfelder S, Jessberger G, Muhar M, Hossain MJ, et al: **Topologically associating domains and chromatin loops depend on cohesin and are regulated by CTCF, WAPL, and PDS5 proteins.** *EMBO J* 2017, **36:**3573-3599.
22. Haarhuis JH, Rowland BD: **Cohesin: building loops, but not compartments.** *EMBO J* 2017, **36:**3549-3551.
23. Cremer M, Cremer T: **Nuclear compartmentalization, dynamics, and function of regulatory DNA sequences.** *Genes Chromosomes Cancer* 2019, **58:**427-436.

24. Cremer T, Cremer M, Hubner B, Strickfaden H, Smeets D, Popken J, Sterr M, Markaki Y, Rippe K, Cremer C: **The 4D nucleome: Evidence for a dynamic nuclear landscape based on co-aligned active and inactive nuclear compartments.** *FEBS Lett* 2015, **589:**2931-2943.
25. Cremer T, Strickfaden H, Cremer M, Hübner B, Silahtaroglu A, Hendzel M, Lanctot C, Cremer C: **Functional nuclear organization: The interchromatin compartment is shaped by dynamic chromatin arrangements.** *BioEssays, in press* 2019.
26. Rouquette J, Cremer C, Cremer T, Fakan S: **Functional nuclear architecture studied by microscopy: present and future.** *Int Rev Cell Mol Biol* 2010, **282:**1-90.
27. Pope BD, Ryba T, Dileep V, Yue F, Wu W, Denas O, Vera DL, Wang Y, Hansen RS, Canfield TK, et al: **Topologically associating domains are stable units of replication-timing regulation.** *Nature* 2014, **515:**402-405.
28. Oldach P, Nieduszynski CA: **Cohesin-Mediated Genome Architecture Does Not Define DNA Replication Timing Domains.** *Genes (Basel)* 2019, **10**.
29. Sima J, Chakraborty A, Dileep V, Michalski M, Klein KN, Holcomb NP, Turner JL, Paulsen MT, Rivera-Mulia JC, Trevilla-Garcia C, et al: **Identifying cis Elements for Spatiotemporal Control of Mammalian DNA Replication.** *Cell* 2019, **176:**816-830 e818.
30. Cremer M, Grasser F, Lanctot C, Muller S, Neusser M, Zinner R, Solovei I, Cremer T: **Multicolor 3D fluorescence in situ hybridization for imaging interphase chromosomes.** *Methods Mol Biol* 2008, **463:**205-239.
31. Jevtic P, Edens LJ, Vukovic LD, Levy DL: **Sizing and shaping the nucleus: mechanisms and significance.** *Curr Opin Cell Biol* 2014, **28:**16-27.
32. Langer S, Geigl JB, Ehnle S, Gangnus R, Speicher MR: **Live cell catapulting and recultivation does not change the karyotype of HCT116 tumor cells.** *Cancer Genet Cytogenet* 2005, **161:**174-177.
33. Melcher R, Koehler S, Steinlein C, Schmid M, Mueller CR, Luehrs H, Menzel T, Scheppach W, Moerk H, Scheurlen M, et al: **Spectral karyotype analysis of colon cancer cell lines of the tumor suppressor and mutator pathway.** *Cytogenet Genome Res* 2002, **98:**22-28.
34. Schmid VJ, Cremer M, Cremer T: **Quantitative analyses of the 3D nuclear landscape recorded with super-resolved fluorescence microscopy.** *Methods* 2017, **123:**33-46.
35. Lin S, Coutinho-Mansfield G, Wang D, Pandit S, Fu XD: **The splicing factor SC35 has an active role in transcriptional elongation.** *Nat Struct Mol Biol* 2008, **15:**819-826.
36. Spector DL, Lamond AI: **Nuclear speckles.** *Cold Spring Harb Perspect Biol* 2011, **3**.
37. Egloff S, Murphy S: **Cracking the RNA polymerase II CTD code.** *Trends Genet* 2008, **24:**280-288.
38. Zhou VW, Goren A, Bernstein BE: **Charting histone modifications and the functional organization of mammalian genomes.** *Nat Rev Genet* 2011, **12:**7-18.
39. Dimitrova DS, Berezney R: **The spatio-temporal organization of DNA replication sites is identical in primary, immortalized and transformed mammalian cells.** *J Cell Sci* 2002, **115:**4037-4051.
40. Chagin VO, Stear JH, Cardoso MC: **Organization of DNA replication.** *Cold Spring Harb Perspect Biol* 2010, **2:**a000737.
41. Jackson DA, Pombo A: **Replicon clusters are stable units of chromosome structure: evidence that nuclear organization contributes to the efficient activation and propagation of S phase in human cells.** *J Cell Biol* 1998, **140:**1285-1295.
42. Schermelleh L, Solovei I, Zink D, Cremer T: **Two-color fluorescence labeling of early and mid-to-late replicating chromatin in living cells.** *Chromosome Res* 2001, **9:**77-80.
43. Zink D, Bornfleth H, Visser A, Cremer C, Cremer T: **Organization of early and late replicating DNA in human chromosome territories.** *Exp Cell Res* 1999, **247:**176-188.
44. Xiang W, Roberti MJ, Heriche JK, Huet S, Alexander S, Ellenberg J: **Correlative live and super-resolution imaging reveals the dynamic structure of replication domains.** *J Cell Biol* 2018, **217:**1973-1984.
45. Heng HH, Goetze S, Ye CJ, Liu G, Stevens JB, Bremer SW, Wykes SM, Bode J, Krawetz SA: **Chromatin loops are selectively anchored using scaffold/matrix-attachment regions.** *J Cell Sci* 2004, **117:**999-1008.
46. Diaz-Martinez LA, Beauchene NA, Furniss K, Esponda P, Gimenez-Abian JF, Clarke DJ: **Cohesin is needed for bipolar mitosis in human cells.** *Cell Cycle* 2010, **9:**1764-1773.
47. Hintermair C, Voss K, Forne I, Heidemann M, Flatley A, Kremmer E, Imhof A, Eick D: **Specific threonine-4 phosphorylation and function of RNA polymerase II CTD during M phase progression.** *Sci Rep* 2016, **6:**27401.
48. Giebel B, Punzel M: **Lineage development of hematopoietic stem and progenitor cells.** *Biol Chem* 2008, **389:**813-824.

49. Joos S, Granzow M, Holtgreve-Grez H, Siebert R, Harder L, Martin-Subero JI, Wolf J, Adamowicz M, Barth TF, Lichter P, Jauch A: **Hodgkin's lymphoma cell lines are characterized by frequent aberrations on chromosomes 2p and 9p including REL and JAK2.** *Int J Cancer* 2003, **103:**489-495.
50. Takaki T, Montagner M, Serres MP, Le Berre M, Russell M, Collinson L, Szuhai K, Howell M, Boulton SJ, Sahai E, Petronczki M: **Actomyosin drives cancer cell nuclear dysmorphia and threatens genome stability.** *Nat Commun* 2017, **8:**16013.
51. Zwerger M, Ho CY, Lammerding J: **Nuclear mechanics in disease.** *Annu Rev Biomed Eng* 2011, **13:**397-428.
52. Moindrot B, Audit B, Klous P, Baker A, Thermes C, de Laat W, Bouvet P, Mongelard F, Arneodo A: **3D chromatin conformation correlates with replication timing and is conserved in resting cells.** *Nucleic Acids Res* 2012, **40:**9470-9481.
53. Zhao PA, Rivera-Mulia JC, Gilbert DM: **Replication Domains: Genome Compartmentalization into Functional Replication Units.** *Adv Exp Med Biol* 2017, **1042:**229-257.
54. Nakamura H, Morita T, Sato C: **Structural organizations of replicon domains during DNA synthetic phase in the mammalian nucleus.** *Exp Cell Res* 1986, **165:**291-297.
55. Baddeley D, Chagin VO, Schermelleh L, Martin S, Pombo A, Carlton PM, Gahl A, Domaing P, Birk U, Leonhardt H, et al: **Measurement of replication structures at the nanometer scale using super-resolution light microscopy.** *Nucleic Acids Res* 2010, **38:**e8.
56. Marchal C, Sima J, Gilbert DM: **Control of DNA replication timing in the 3D genome.** *Nat Rev Mol Cell Biol* 2019.
57. Hansen AS, Cattoglio C, Darzacq X, Tjian R: **Recent evidence that TADs and chromatin loops are dynamic structures.** *Nucleus* 2018, **9:**20-32.
58. Wang XT, Dong PF, Zhang HY, Peng C: **Structural heterogeneity and functional diversity of topologically associating domains in mammalian genomes.** *Nucleic Acids Res* 2015, **43:**7237-7246.
59. Zhan Y, Mariani L, Barozzi I, Schulz EG, Bluthgen N, Stadler M, Tiana G, Giorgetti L: **Reciprocal insulation analysis of Hi-C data shows that TADs represent a functionally but not structurally privileged scale in the hierarchical folding of chromosomes.** *Genome Res* 2017, **27:**479-490.
60. Rowley MJ, Corces VG: **Organizational principles of 3D genome architecture.** *Nat Rev Genet* 2018, **19:**789-800.
61. Barrington C, Finn R, Hadjur S: **Cohesin biology meets the loop extrusion model.** *Chromosome Res* 2017, **25:**51-60.
62. Fudenberg G, Abdennur N, Imakaev M, Goloborodko A, Mirny LA: **Emerging Evidence of Chromosome Folding by Loop Extrusion.** *Cold Spring Harb Symp Quant Biol* 2017, **82:**45-55.
63. Nuebler J, Fudenberg G, Imakaev M, Abdennur N, Mirny LA: **Chromatin organization by an interplay of loop extrusion and compartmental segregation.** *Proc Natl Acad Sci U S A* 2018, **115:**E6697-E6706.
64. Richterova J, Huraiova B, Gregan J: **Genome Organization: Cohesin on the Move.** *Mol Cell* 2017, **66:**444-445.
65. Naumova N, Imakaev M, Fudenberg G, Zhan Y, Lajoie BR, Mirny LA, Dekker J: **Organization of the mitotic chromosome.** *Science* 2013, **342:**948-953.
66. Gibcus JH, Samejima K, Goloborodko A, Samejima I, Naumova N, Nuebler J, Kanemaki MT, Xie L, Paulson JR, Earnshaw WC, et al: **A pathway for mitotic chromosome formation.** *Science* 2018, **359**.
67. Bernardi G: **Genome Organization and Chromosome Architecture.** *Cold Spring Harb Symp Quant Biol* 2015, **80:**83-91.
68. Jabbari K, Bernardi G: **An Isochore Framework Underlies Chromatin Architecture.** *PLoS One* 2017, **12:**e0168023.
69. Mirny LA, Imakaev M, Abdennur N: **Two major mechanisms of chromosome organization.** *Curr Opin Cell Biol* 2019, **58:**142-152.
70. Sexton T, Yaffe E, Kenigsberg E, Bantignies F, Leblanc B, Hoichman M, Parrinello H, Tanay A, Cavalli G: **Three-dimensional folding and functional organization principles of the Drosophila genome.** *Cell* 2012, **148:**458-472.
71. Bintu B, Mateo LJ, Su JH, Sinnott-Armstrong NA, Parker M, Kinrot S, Yamaya K, Boettiger AN, Zhuang X: **Super-resolution chromatin tracing reveals domains and cooperative interactions in single cells.** *Science* 2018, **362**.

72. Nir G, Farabella I, Perez Estrada C, Ebeling CG, Beliveau BJ, Sasaki HM, Lee SD, Nguyen SC, McCole RB, Chattoraj S, et al: **Walking along chromosomes with super-resolution imaging, contact maps, and integrative modeling.** *PLoS Genet* 2018, **14:**e1007872.
73. Dekker J, Belmont AS, Guttman M, Leshyk VO, Lis JT, Lomvardas S, Mirny LA, O'Shea CC, Park PJ, Ren B, et al: **The 4D nucleome project.** *Nature* 2017, **549:**219-226.
74. Finn EH, Pegoraro G, Brandao HB, Valton AL, Oomen ME, Dekker J, Mirny L, Misteli T: **Extensive Heterogeneity and Intrinsic Variation in Spatial Genome Organization.** *Cell* 2019, **176:**1502-1515 e1510.
75. Krumm A, Duan Z: **Understanding the 3D genome: Emerging impacts on human disease.** *Semin Cell Dev Biol* 2019, **90:**62-77.
76. Szabo Q, Bantignies F, Cavalli G: **Principles of genome folding into topologically associating domains.** *Sci Adv* 2019, **5:**eaaw1668.
77. Otterstrom J, Castells-Garcia A, Vicario C, Gomez-Garcia PA, Cosma MP, Lakadamyali M: **Super-resolution microscopy reveals how histone tail acetylation affects DNA compaction within nucleosomes in vivo.** *Nucleic Acids Res* 2019.
78. Ricci MA, Manzo C, Garcia-Parajo MF, Lakadamyali M, Cosma MP: **Chromatin fibers are formed by heterogeneous groups of nucleosomes in vivo.** *Cell* 2015, **160:**1145-1158.
79. Xu J, Liu Y: **A guide to visualizing the spatial epigenome with super-resolution microscopy.** *FEBS J* 2019.
80. Maeshima K, Kaizu K, Tamura S, Nozaki T, Kokubo T, Takahashi K: **The physical size of transcription factors is key to transcriptional regulation in chromatin domains.** *J Phys Condens Matter* 2015, **27:**064116.
81. Maeshima K, Ide S, Babokhov M: **Dynamic chromatin organization without the 30-nm fiber.** *Curr Opin Cell Biol* 2019, **58:**95-104.
82. Maeshima K, Rogge R, Tamura S, Joti Y, Hikima T, Szerlong H, Krause C, Herman J, Seidel E, DeLuca J, et al: **Nucleosomal arrays self-assemble into supramolecular globular structures lacking 30-nm fibers.** *EMBO J* 2016, **35:**1115-1132.
83. Paulsen J, Liyakat Ali TM, Nekrasov M, Delbarre E, Baudement MO, Kurscheid S, Tremethick D, Collas P: **Long-range interactions between topologically associating domains shape the four-dimensional genome during differentiation.** *Nat Genet* 2019, **51:**835-843.
84. Nmezi B, Xu J, Fu R, Armiger TJ, Rodriguez-Bey G, Powell JS, Ma H, Sullivan M, Tu Y, Chen NY, et al: **Concentric organization of A- and B-type lamins predicts their distinct roles in the spatial organization and stability of the nuclear lamina.** *Proc Natl Acad Sci U S A* 2019.
85. Szczurek A, Klewes L, Xing J, Gourram A, Birk U, Knecht H, Dobrucki JW, Mai S, Cremer C: **Imaging chromatin nanostructure with binding-activated localization microscopy based on DNA structure fluctuations.** *Nucleic Acids Res* 2017, **45:**e56.
86. Lleres D, Bailly AP, Perrin A, Norman DG, Xirodimas DP, Feil R: **Quantitative FLIM-FRET Microscopy to Monitor Nanoscale Chromatin Compaction In Vivo Reveals Structural Roles of Condensin Complexes.** *Cell Rep* 2017, **18:**1791-1803.
87. Lou J, Scipioni L, Wright BK, Bartolec TK, Zhang J, Masamsetti VP, Gaus K, Gratton E, Cesare AJ, Hinde E: **Phasor histone FLIM-FRET microscopy quantifies spatiotemporal rearrangement of chromatin architecture during the DNA damage response.** *Proc Natl Acad Sci U S A* 2019, **116:**7323-7332.
88. Pelicci S, Diaspro A, Lanzano L: **Chromatin nanoscale compaction in live cells visualized by acceptor-to-donor ratio corrected Forster resonance energy transfer between DNA dyes.** *J Biophotonics* 2019**:**e201900164.
89. Priest DG, Solano A, Lou J, Hinde E: **Fluorescence fluctuation spectroscopy: an invaluable microscopy tool for uncovering the biophysical rules for navigating the nuclear landscape.** *Biochem Soc Trans* 2019, **47:**1117-1129.
90. Markaki Y, Smeets D, Cremer M, Schermelleh L: **Fluorescence in situ hybridization applications for super-resolution 3D structured illumination microscopy.** *Methods Mol Biol* 2013, **950:**43-64.
91. Schermelleh L: **In Vivo DNA replication labeling.** *Cell Biology - a laboratory handbook* 2006, **3rd edition volume 1, editor J.E. Celis, Elsevier Academic Press**
92. Clarke ST, Song Z, Kwan KY, DeMarco C, Rukavishnikov A, Singh U, Gee K: **GFP compatibility with EdU cell proliferation assay.** *DOI: 101158/1538-7445AM2014-5098* 2014.
93. Salic A, Mitchison TJ: **A chemical method for fast and sensitive detection of DNA synthesis in vivo.** *Proc Natl Acad Sci U S A* 2008, **105:**2415-2420.
94. Durand NC, Robinson JT, Shamim MS, Machol I, Mesirov JP, Lander ES, Aiden EL: **Juicebox Provides a Visualization System for Hi-C Contact Maps with Unlimited Zoom.** *Cell Syst* 2016, **3:**99-101.

95. Durand NC, Shamim MS, Machol I, Rao SS, Huntley MH, Lander ES, Aiden EL: **Juicer Provides a One-Click System for Analyzing Loop-Resolution Hi-C Experiments.** *Cell Syst* 2016, **3:**95-98.
96. Javanmoghadam-Kamrani S, Keyomarsi K: **Synchronization of the cell cycle using lovastatin.** *Cell Cycle* 2008, **7:**2434-2440.
97. Marchal C, Sasaki T, Vera D, Wilson K, Sima J, Rivera-Mulia JC, Trevilla-Garcia C, Nogues C, Nafie E, Gilbert DM: **Genome-wide analysis of replication timing by next-generation sequencing with E/L Repli-seq.** *Nat Protoc* 2018, **13:**819-839.
98. Guillou E, Ibarra A, Coulon V, Casado-Vela J, Rico D, Casal I, Schwob E, Losada A, Mendez J: **Cohesin organizes chromatin loops at DNA replication factories.** *Genes Dev* 2010, **24:**2812-2822.
99. Schindelin J, Arganda-Carreras I, Frise E, Kaynig V, Longair M, Pietzsch T, Preibisch S, Rueden C, Saalfeld S, Schmid B, et al: **Fiji: an open-source platform for biological-image analysis.** *Nat Methods* 2012, **9:**676-682.
100. Dobbie IM, King E, Parton RM, Carlton PM, Sedat JW, Swedlow JR, Davis I: **OMX: a new platform for multimodal, multichannel wide-field imaging.** *Cold Spring Harb Protoc* 2011, **2011:**899-909.
101. Pau G, Fuchs F, Sklyar O, Boutros M, Huber W: **EBImage--an R package for image processing with applications to cellular phenotypes.** *Bioinformatics* 2010, **26:**979-981.
102. R Core Team: **R: A language and environment for statistical computing.** In *Book R: A language and environment for statistical computing* (Editor ed.^eds.). City: R Foundation for Statistical Computing, Vienna, Austria; 2013.

Authors contributions

TC and ELA initiated the study; MC and TC conceived the microscopic experiments together with HH; KB, MC and AM performed experiments shown in Figs. 1- 4,6 - 7 and Suppl. Figs. 2- 4. AM and KB performed live cell and super-resolution/confocal microscopy; HH provided input on quantitative image analysis, including statistical analysis; AM performed segmentation analyses and VS 3D image analyses for chromatin density mapping data; SM performed DNA Halo experiments with support of MCC. Hi-C data were generated by SSPR and ELA with experimental support of NM (Fig. 5). Repli-Seq data were provided by DMG and KNK. HL provided input for the 3D imaging part and MCC for the replication part. MC and TC wrote the manuscript with support from all authors, in particular from ELA.

Competing interests

The authors declare to have no competing interests.

Availability of supporting data

All data generated or analyzed during this study are included in this published article and its Additional files.

Consent for publication

All authors read and approved the manuscript.

Ethical approval and consent to participate

Not applicable

Funding

This work was supported by grants of the Deutsche Forschungsgemeinschaft (GRK1657/TP1C and CA198/9-2) to MCC and by the DFG Priority Programm SPP 2202 to HH and HL. ELA was supported by an NSF Physics Frontiers Center Award (PHY1427654), the Welch Foundation (Q-1866), a USDA Agriculture and Food Research Initiative Grant (2017-05741), an NIH 4D Nucleome Grant (U01HL130010), and an NIH Encyclopedia of DNA Elements Mapping Center Award (UM1HG009375).